Dynamics of Energetic Heliospheric Ions in Pluto's Induced Magnetosphere

Randall T. Ruch[1], **Sven Simon**[1,2], **C. Michael Haynes**[1]

[1]School of Earth and Atmospheric Sciences, Georgia Institute of Technology, Atlanta, GA, USA

[2]School of Physics, Georgia Institute of Technology, Atlanta, GA, USA

Key Points:

- We model the dynamics of energetic heliospheric ions that travel through the draped electromagnetic fields of Pluto's induced magnetosphere
- Deflection of energetic ions by the dwarf planet's induced magnetosphere generates flux perturbations as far as 200 Pluto radii downstream
- The modeled depletions in energetic ion flux downstream of Pluto are weaker than those observed in this region during the New Horizons flyby

Corresponding author: Randall T. Ruch, `randy.ruch@eas.gatech.edu`

Abstract

We present a model of the interaction between energetic heliospheric ions and Pluto's induced magnetosphere. The electromagnetic fields near the dwarf planet are highly non-uniform, displaying extended signatures of pile-up and draping. While the induced magnetosphere possesses a downstream extension above 100 Pluto radii, the weak interplanetary magnetic field in the outer heliosphere leads energetic ions to gyrate on comparable length scales. We obtain the three-dimensional structure of the fields near Pluto using a hybrid model, and a particle tracing tool is applied to study the dynamics of energetic ions traveling through these fields. For multiple initial energies, we compute the ion fluxes through a plane detector downstream of Pluto. Our results are as follows: (a) Deflection by Pluto's induced magnetosphere causes highly non-uniform perturbations in the flux pattern of energetic ions at its downstream side. These patterns include regions where the fluxes are increased or reduced by up to 40%, compared to the values in uniform fields. (b) Consistent with findings from New Horizons, the modeled perturbations gradually diminish with distance downstream of the dwarf planet out to 200 Pluto radii. (c) The deflection of the energetic ions mainly occurs within regions of Pluto's induced magnetosphere where the magnetic field is significantly enhanced, thereby causing a localized reduction in gyroradii. (d) The magnitude of the depletion in flux in our steady-state model is weaker than seen by New Horizons; this may suggest that time-dependent processes in Pluto's wake (e.g., bi-ion waves) play a major role in deflecting these ions.

1 Introduction

Pluto (radius $R_P = 1,188$ km), formerly considered the ninth planet of our solar system, is a Kuiper belt object with an eccentric orbit around the Sun ranging in radial distance from 30 to 49 AU. Its atmosphere was first detected via stellar occultation in 1988 (Hubbard et al., 1988) and is generated by the evaporation of volatile ices, including nitrogen (N_2) and methane (CH_4), on the surface (Owen et al., 1993). Methane has been detected by Young et al. (1997), but was concluded to be only a minor atmospheric constituent. Instead, Owen et al. (1993) suggested that nitrogen is the most abundant atmospheric species due to the prevalence of N_2 ice on Pluto's surface. Initial model results for a hydrodynamically escaping atmosphere—in which N_2 is entrained in a planetary wind of escaping CH_4—yielded neutral gas temperatures of more than 90 K out

to 1 R_P altitude (Krasnopolsky, 1999; Krasnopolsky & Cruikshank, 1999). Estimated escape rates of the neutral species are on the order of 10^{27} s^{-1} for N_2 and 10^{26}-10^{27} s^{-1} for CH_4 (Krasnopolsky, 1999).

The New Horizons (NH) spacecraft encountered Pluto on July 14, 2015 at a distance of 33 AU from the Sun. Its trajectory was inclined against Pluto's orbital plane by about 3°. The spacecraft crossed the plane from the south (below) to the north (above) as its trajectory intersected the Sun-Pluto line about 45 R_P downstream of the dwarf planet (Bagenal et al., 2016). Observations from this flyby have found Pluto's upper atmosphere to be much colder than suggested by earlier, remote observations: data from the *Alice* UV spectrometer aboard NH revealed neutral gas temperatures of less than 70 K out to altitudes more than 1 R_P (Gladstone et al., 2016). Additionally, Pluto's atmosphere at the time of the flyby was not undergoing substantial hydrodynamic escape: only thermal (Jeans) escape of neutrals and loss through ionization were occurring (Gladstone et al., 2016; McComas et al., 2016). Due to the lower temperature, the escape rates derived from NH data are orders of magnitude below those estimated prior to the flyby: 10^{23} s^{-1} for N_2 and $5{\cdot}10^{25}$ s^{-1} for CH_4 (Gladstone et al., 2016). Additionally, CH_4 was found to be the dominant constituent of the atmosphere at altitudes greater than 1 R_P where N_2 densities become rarefied.

The ionization of neutral N_2 and CH_4 in Pluto's upper atmosphere via charge exchange with solar wind protons and photoionization via solar extreme ultraviolet (EUV) photons yields N_2^+ and CH_4^+ ions (Cravens & Strobel, 2015). The production of these heavy (Plutogenic) ions generates the dwarf planet's ionosphere, representing an obstacle to the solar wind flow. The drain of momentum from the solar wind due to the pickup of heavy ions from the ionosphere decelerates the impinging flow and leads to perturbations of the electromagnetic fields, generating the dwarf planet's induced magnetosphere (e.g., Delamere, 2009). The abrupt deceleration of the supermagnetosonic solar wind flow (magnetosonic Mach number $M_{MS} \approx 10$) gives rise to a bow shock upstream of Pluto (Bagenal et al., 2016; McComas et al., 2016). An ion composition boundary called the *Plutopause* is formed between the solar wind and heavy ion populations. The Plutopause encases an extensive heavy ion tail largely devoid of SW ions (McComas et al., 2016).

Since the interplanetary magnetic field (IMF) strength decreases with distance from the Sun, heavy pickup ion gyroradii near Pluto become two to three orders of magni-

tude larger than the dwarf planet itself (Bagenal et al., 2015). At Pluto's orbit, the IMF is expected to be (on average) either parallel or antiparallel to the direction of the dwarf planet's orbital motion; i.e., it is perpendicular to the bulk velocity of the impinging solar wind. The direction of the ambient convective electric field depends on the orientation of the IMF: $\vec{E}_0 = -\vec{u}_0 \times \vec{B}_0$, where $\vec{u}_0$ is the upstream solar wind velocity and $\vec{B}_0$ is the IMF vector. An IMF oriented antiparallel to Pluto's orbital motion generates a convective electric field pointing northward, and vice versa. Freshly picked-up heavy ions begin their cycloidal motion by streaming along the electric field with near-ballistic trajectories due to their large gyroradii (e.g., Feyerabend et al., 2017). To conserve momentum, the solar wind flow is redirected opposite the motion of the pickup ions. Consequently, a strong north-south asymmetry arises in the plasma flow pattern and the electromagnetic fields near Pluto (e.g., Delamere, 2009; Feyerabend et al., 2017). A similar north-south asymmetry was seen in the ion tail during the AMPTE experiment that emulated an artificial comet (e.g., Valenzuela et al., 1986; Coates et al., 1988; Delamere et al., 1999).

New Horizons was equipped with multiple instruments that measured Pluto's plasma environment. The *Solar Wind Around Pluto* (SWAP) instrument detects ions with energy-per-charge ratios (E/q) ranging from 0.035 to 7.5 keV/q (McComas et al., 2007), allowing the derivation of solar wind parameters, such as flow speed, density, and temperature. The solar wind observed by SWAP during the flyby was very tenuous with a proton density of 0.025 cm^{-3} (versus about 5 cm^{-3} at 1 AU) and an upstream bulk velocity of 403 km/s (Bagenal et al., 2016). McComas et al. (2016) analyzed the solar wind slowing to identify a standoff distance for the bow shock of 4.5 R_P upstream of Pluto's center.

New Horizons did not carry a magnetometer, so it did not directly measure the strength or direction of the IMF near Pluto. Prior to the flyby, Bagenal et al. (2015) examined Voyager 2 data from distances of 25 AU to 39 AU to determine a range of 0.08 nT to 0.28 nT for the IMF strength at 33 AU (corresponding to pickup N_2^+ gyroradii of about 1250 R_P to about 350 R_P, respectively). The direction of the IMF at the time of the flyby has been inferred indirectly by using SWAP counts of heavy pickup ions (Zirnstein et al., 2016; McComas et al., 2016). The instrument's field-of-view was oriented such that it could simultaneously measure ions entering the detector from regions north and south of the Sun-Pluto line. Zirnstein et al. (2016) constructed a model that calculated the trajectories of heavy ions which entered SWAP at the time of the flyby to determine the

IMF orientation. They demonstrated that only an outward IMF sector—i.e., $\vec{B}_0$ oriented antiparallel to Pluto's orbital direction—could explain SWAP heavy ion counts. The resulting convective electric field, $\vec{E}_0$, would point northward such that heavy pickup ions streaming along the electric field would redirect the solar wind flow toward the south.

The large gyroradii of Plutogenic pickup ions suggest that any model of the dwarf planet's interaction with the solar wind must account for both flow shear between ion species of different masses and significant asymmetries in the magnetic field topology. Hybrid models (kinetic ions, fluid electrons) and multi-fluid models have been applied to study Pluto's plasma environment. Harnett et al. (2005) demonstrated that both methods are capable of qualitatively capturing the impact of ion gyration on the flow pattern and electromagnetic fields. Discrepancies between the two methods arise in the extent of the pickup tail, since the multi-fluid model does not capture the dynamics of individual ions.

Prior to the NH encounter, Delamere and Bagenal (2004) studied Pluto's interaction with the solar wind using a three-dimensional hybrid model (kinetic ions, fluid electrons). These authors assumed that there was significant hydrodynamic outflow of Pluto's atmosphere and that N_2 was the dominant escaping species. This model was expanded upon by Delamere (2009); the previous iteration had made physical compromises for computational efficiency, such as setting the mass of N_2^+ ions to 10 proton masses. Delamere (2009) simulated Pluto's interaction region for three atmospheric N_2 escape rates: $Q_1 = 2{\cdot}10^{26}$ s^{-1}, $Q_2 = 2{\cdot}10^{27}$ s^{-1}, and $Q_3 = 2{\cdot}10^{28}$ s^{-1}. In their model, Pluto's ionosphere is generated through photoionization and the charge exchange reaction $H^+ + N_2 \rightarrow H + N_2^+$. The different neutral escape rates proved to have a significant effect on the shape of the bow shock. As the neutral outflow rate increased from Q_1 to Q_3, the modeled shock structures transitioned from a Mach cone, to a weak shock (attached to Pluto's ionosphere), and finally to a fully detached bow shock. Additionally, Delamere (2009) found significant structuring in the plasma at the wakeside of Pluto due to the presence of bi-ion waves arising from flow shear between the solar wind and heavy pickup ions.

Data from the NH encounter revealed that Pluto's atmosphere is colder, more confined, and CH_4 dominated (at altitudes greater than 1 R_P). Therefore, post-NH hybrid models have employed in-situ atmospheric observations (e.g., Gladstone et al., 2016; Young et al., 2017) for representing the dwarf planet's neutral envelope. Feyerabend et al. (2017)

included NH encounter estimates of solar wind and atmospheric parameters in their hybrid simulations of Pluto's induced magnetosphere. A major goal of their study was to constrain the strength and direction of the IMF at the time of the flyby. Their model included neutral profiles of N_2 and CH_4 extrapolated from atmospheric observations of Gladstone et al. (2016). They considered five different model setups with varying IMF strength and orientation. Four of these simulations used the following values for $|\vec{B}_0|$, covering the range observed by Voyager 2 near 33 AU (Bagenal et al., 2015): 0.08 nT, 0.16 nT, 0.24 nT, and 0.30 nT. These four runs included an IMF oriented antiparallel to Pluto's orbital motion, consistent with the conclusions of Zirnstein et al. (2016) and McComas et al. (2016). The fifth simulation used an IMF strength of 0.30 nT but oriented oppositely. Feyerabend et al. (2017) constrained the IMF magnitude by comparing the solar wind flow speed output by their model to SWAP measurements of the solar wind slowing profile near Pluto's bow shock (McComas et al., 2016). Their model revealed that the slowing profile of the solar wind strongly depends on IMF strength, with a magnitude of at least 0.24 nT needed to reproduce SWAP observations. Both simulations with an IMF strength of 0.30 nT were able to quantitatively reproduce the measured solar wind speeds, regardless of field orientation.

The hybrid model of Barnes et al. (2019) was used with a similar goal of constraining the strength of the IMF at Pluto during the NH flyby. In contrast to, e.g., Delamere (2009) or Feyerabend et al. (2017), their setup includes multiple upstream ion populations: one Maxwellian distribution of solar wind protons, one Maxwellian distribution of doubly-charged alpha particles (He^{++}) with one-tenth the number density of the protons, and a drifting spherical shell distribution of protons with a number density similar to that of the alpha particles. The latter population represents interstellar pickup ions, which arise from the ionization and pickup of interstellar gas. The atmospheric model used in their hybrid simulations consists of a neutral profile of CH_4 extrapolated from Young et al. (2017). However, Barnes et al. (2019) assumed methane to be the only significant constituent of Pluto's upper atmosphere. These authors created a numerical model of the SWAP instrument's response to incoming ions, allowing them to generate synthetic time series from the output of their hybrid model.

Barnes et al. (2019) identify three observables that depend on IMF strength: heavy pickup ion energy, the width of the heavy ion tail, and the profile of thermal pressure along the NH trajectory. Their model does not show the same dependence of the solar

wind slowing profile on IMF strength as Feyerabend et al. (2017). They infer a value for IMF strength of less than 0.1 nT. The inclusion of only a single upstream species by Feyerabend et al. (2017) means pressure balance at the Plutopause would have to be accounted for by increased magnetic pressure, leading to a larger value for IMF strength than concluded by Barnes et al. (2019). The models of Feyerabend et al. (2017) and Barnes et al. (2019) both reproduce the solar wind slowing pattern observed by SWAP; i.e., the location and thickness of the bow shock is consistent between the two. In both models, the ionospheric obstacle presented to the solar wind flow is less than about 10 R_P in diameter.

In addition to solar wind and Plutogenic pickup ions, the dwarf planet is embedded in a population of energetic heliospheric ions—with energies from a few to hundreds of keV—constituted by interstellar pickup and suprathermal ions (Kollmann, Hill, Allen, et al., 2019). The gyroradii of singly-charged helium ions in this population range from 45 R_P at 2 keV to 321 R_P at 100 keV for an IMF magnitude of 0.24 nT. The interstellar pickup ions are accelerated along the convective electric field to drift with the bulk velocity of the solar wind as they gyrate (Kollmann, Hill, McNutt, et al., 2019). Interstellar pickup proton and helium ion energies cutoff at a maximum of twice the flow speed in the Sun's rest frame, when their gyration conspires entirely in the direction of their drift. Thus, they populate the energy range up to 3.4 keV for protons and 13.6 keV for helium ions. The suprathermal population arises from interstellar pickup ions that have undergone further acceleration, and it accounts for the range of energies above the pickup ion cutoffs. The mechanism for this acceleration is still debated (Fisk & Gloeckler, 2012; Randol & Christian, 2014; Kollmann, Hill, McNutt, et al., 2019).

The *Pluto Energetic Particle Spectrometer Science Investigation* (PEPSSI) instrument onboard NH measured the differential intensity (number flux per energy per steradian) of the He^+ component of the energetic heliospheric ion distribution. Shortly after closest approach, as NH was 8-9 R_P downstream of Pluto (at a radial distance of 13 R_P from its center), the PEPSSI instrument observed an increase in the differential intensity of the energetic ion flux above the nominal interplanetary level, despite the instrument's look direction pointing away from the Sun. This enhancement was followed by an order-of-magnitude reduction in differential intensity which immediately began to replenish exponentially over an estimated distance of 190 R_P downstream (Kollmann, Hill, Allen, et al., 2019). The initial increase is interpreted by Bagenal et al. (2016) as the energetic ions being deflected by Pluto's induced magnetosphere. The subsequent

reduction of differential intensity is indicative of an energetic particle wake formed downstream of Pluto. Since the length scales of energetic ion motion are up to an order-of-magnitude larger than the obstacle that Pluto presents to the solar wind (Feyerabend et al., 2017; Barnes et al., 2019), it is unclear why the dwarf planet has such an extreme influence on the dynamics of these particles. The physical mechanisms leading to the energetic ion depletion observed by NH have yet to be determined. Additionally, the differential intensity of the energetic ions within the depleted wake region was observed to oscillate with a periodicity of about 0.2 hours. Kollmann, Hill, Allen, et al. (2019) suggest a possible cause being deflection of the energetic ions by ultra-low frequency plasma waves, such as bi-ion waves that stem from the relative motion of solar wind and ionospheric ions.

The goal of our study is to investigate the cause of the observed depletion of the energetic heliospheric ion population downstream of Pluto. To accomplish this, we calculate the three-dimensional structure of the electromagnetic fields in Pluto's induced magnetosphere during the NH flyby using the AIKEF hybrid model (Müller et al., 2011). The field output from the hybrid model is then incorporated into a newly developed particle tracing simulation of the energetic He^+ population incident upon Pluto's interaction region. This paper has the following structure: the use of the hybrid model is discussed in section 2.1, and the energetic ion tracer is described in sections 2.2 and 2.3. The results of these models are discussed in section 3. A summary and conclusion are found in section 4.

2 Hybrid Model and Energetic Ion Tracer

A Pluto-centered, Cartesian coordinate system (x, y, z) is introduced for the modeling of the dwarf planet's induced magnetosphere and tracing of energetic heliospheric ions. The x-axis coincides with the Sun-Pluto line and points anti-sunward from the dwarf planet. The y-axis is oriented in the direction of Pluto's orbital motion. The z-axis is directed northward of the orbital plane to complete the right-handed coordinate system.

2.1 Modeling of Pluto's Induced Magnetosphere

To calculate the electromagnetic field perturbations generated by Pluto's interaction with the solar wind, we apply the AIKEF hybrid model (Müller et al., 2011). In this

model, ions are treated as individual macroparticles, representing some number of real ions with similar positions in phase space. The kinetic treatment of ions is necessary for interactions involving non-Maxwellian velocity distributions (caused by, e.g., ion pickup) and flow shear between impinging and ionospheric ion populations. Both features are critical in shaping Pluto's interaction region, since the gyroradii of solar wind protons and pickup N_2^+ ions are at least 12 R_P and 330 R_P, respectively (e.g., Bagenal et al., 2015). In AIKEF, electrons are treated as a massless, charge-neutralizing fluid. The fluid treatment of electrons is valid near Pluto, since their gyroradii in the ambient solar wind field are less than 0.01 R_P—nearly three orders of magnitude smaller than the obstacle represented by the dwarf planet's ionosphere. The AIKEF model has been employed previously at Pluto to constrain the IMF strength during the NH flyby (Feyerabend et al., 2017). In addition, the model has a 20-year history of application to various other small bodies in the solar system, such as Titan (e.g., Simon et al., 2006; Tippens et al., 2022, 2024), Europa (e.g., Addison et al., 2021, 2022, 2023, 2024; Haynes et al., 2023), Callisto (e.g., Liuzzo et al., 2015, 2016, 2017; Liuzzo, Poppe, et al., 2024), and Ganymede (e.g., Stahl et al., 2023). The output of the model is a three-dimensional data cuboid of the electromagnetic field vectors.

Here, we provide only a brief overview of the parameters used for our Pluto study. Analogous to Feyerabend et al. (2017), we assume the ion population in the impinging solar wind to consist of protons, with their velocities described by a drifting Maxwellian distribution. The values characterizing the upstream solar wind are taken from SWAP data interpreted by Bagenal et al. (2016), namely: a solar wind speed $u_0 = 403$ km/s in the $(+x)$ direction, a proton number density $n_0 = 0.025$ cm^{-3}, and a proton temperature $kT_i = 0.66$ eV. We use an electron temperature of $kT_e = 1$ eV, in agreement with Feyerabend et al. (2017). In our model, the upstream magnetic field $\vec{B}_0$ is oriented antiparallel to Pluto's orbital motion, in the $(-y)$ direction, consistent with the conclusions by Zirnstein et al. (2016) and McComas et al. (2016). We adopt an IMF strength of $|\vec{B}_0| = 0.24$ nT, at the lower bound of the range concluded by Feyerabend et al. (2017), due to our analogous treatment of the upstream plasma. Of the values determined by these authors to be capable of reproducing SWAP measurements, this IMF strength is the most consistent with the range predicted for the NH flyby from Voyager 2 data (Bagenal et al., 2015). This choice of $|\vec{B}_0|$ yields an Alfvén speed of $v_{A,0} = 33$ km/s, an Alfvénic

Mach number $M_A = 12.2$, a solar wind plasma beta $\beta = 0.29$, and a Magnetosonic Mach number $M_{MS} = 10.7$.

The neutral profiles used for N_2 and CH_4 in Pluto's atmosphere are each a sum of barometric laws fit to NH data with parameters given in Table 1 of Feyerabend et al. (2017). Our model includes the ionization of atmospheric neutrals via solar photons and charge exchange. Photoionization is facilitated via the *Extreme UltraViolet flux model for Aeronomic Calculations* (EUVAC) by Richards et al. (1994). The EUVAC model determines the EUV flux across 37 intervals within the UV spectrum to calculate the wavelength-dependent photoionization rates. We include the charge exchange reactions between solar wind protons and the two atmospheric species, $H^+ + N_2 \rightarrow H + N_2^+$, and $H^+ + CH_4 \rightarrow H + CH_4^+$. In our model, the collision frequencies for these charge exchange reactions are spatially non-uniform and given by the product of the local neutral density and a rate coefficient. The rate coefficients for these reactions are 3.36×10^{-9} cm^3 s^{-1} and 4.02×10^{-9} cm^3 s^{-1}, respectively (Schunk & Nagy, 2009). During these reactions, solar wind ions are removed from the simulation and replaced with ionospheric ions.

The particle tracing simulation (section 2.2) will embed the AIKEF field output into a larger domain of uniform electromagnetic fields. To minimize any field gradients at the interface between these two domains, it is important that the field perturbations are weak near the outer boundaries of the AIKEF box. Therefore, the dimensions of our simulation domain are larger than those in Feyerabend et al. (2017) whose study focused solely on Pluto's immediate environment. The extensions of our hybrid simulation domain are 120 R_P in x, and 64 R_P in y and z. The bounds in each direction are [−20, 100] R_P for x, and [−32, 32] R_P for y and z. The ($+x$) direction (i.e., toward downstream) has the largest extent to accommodate for the field line draping. The grid resolution in each dimension is 0.125 R_P. The timestep used in AIKEF is 0.037 s, corresponding to 0.01% of a proton gyroperiod in the ambient solar wind magnetic field.

Initially, each cell of the AIKEF grid is populated with 10 proton macroparticles. For each of the two ionospheric species, 20 macroparticles are injected per timestep into every cell within Pluto's atmosphere. Inflow boundary conditions are used at the upstream ($x = -20$ R_P) and the northern ($z = 32$ R_P) faces of the model domain, whereas outflow conditions are used on the remaining four faces (see Müller et al., 2011, for details). The code applies a 26-point smoothing procedure to the electromagnetic fields in order

to achieve numerical stability (see Müller et al., 2010). Zero divergence of the magnetic field is ensured through the "projection method" described by Müller et al. (2010).

2.2 Tracing of Energetic Heliospheric Ions

This section describes our model used for tracing energetic heliospheric He^+ macroparticles as they travel through Pluto's induced magnetosphere. We have developed this tool to identify the mechanisms responsible for the extensive depletion of energetic ion flux observed downstream of Pluto by NH (Bagenal et al., 2016; Kollmann, Hill, Allen, et al., 2019). The time-of-flight measurements used to identify the downstream depletion in energetic ion flux are dominated by populations of interstellar pickup and suprathermal He^+ ions, with energies ranging from a few keV to more than 100 keV (Kollmann, Hill, Allen, et al., 2019). Shortly after NH's closest approach, PEPSSI data reveal an order of magnitude decrease in energetic ion intensity across this entire energy range when compared to the nominal values observed upstream of the induced magnetosphere. The depletion was first observed near $x = 15\ R_P$ downstream of Pluto and immediately began refilling out to an estimated distance of $x = 190\ R_P$ (Kollmann, Hill, Allen, et al., 2019). In the uniform solar wind outside of Pluto's interaction region, He^+ gyroradii (at pitch angles of 90°) vary from 45 R_P to 321 R_P across the energy range observed by PEPSSI. At the lowest energy, the ion gyroradii are smaller than the size of Pluto's interaction region, whereas at the largest, they are comparable in size. In this study, we present results for the following initial energies (E, in the rest frame of the solar wind) of He^+ ions in our particle tracer: 2 keV, 5 keV, 10 keV, and 20 keV. These values correspond to speeds of 310 to 980 km/s, compared to their $\vec{E}\times\vec{B}$ drift speed (in the undisturbed solar wind) of $u_0 = 403$ km/s. We have also carried out runs at higher energies up to 100 keV. The results of these additional runs were found to merely substantiate the trends that are detailed in section 3.2 for the lower energies, so they are not discussed individually.

The particle tracing simulation uses the three-dimensional electromagnetic field output from the AIKEF hybrid model in the vicinity of Pluto. In other words, the energetic ions analyzed with the particle tracer are treated as test particles that do not influence the electromagnetic fields themselves. Our approach is consistent with the treatment of the energetic He^+ population by Kollmann, Hill, Allen, et al. (2019) who computed the motion of these ions through an analytical representation of the plasma waves that were

suggested to inhabit Pluto's energetic ion wake (e.g., Delamere, 2009; Feyerabend et al., 2017).

The AIKEF simulation cuboid is too small to serve as a standalone simulation domain (dimensions 120 $R_P \times 64\ R_P \times 64\ R_P$): the length of its longest side is less than a third of the distance along the x-axis a He^+ ion would drift in a single gyration, $u_0 P_0 \approx 371\ R_P$. Here, P_0 is the ion gyroperiod in the uniform fields $\vec{E}_0$ and $\vec{B}_0$ outside of Pluto's interaction region. Further, the PEPSSI measurements used to identify the energetic ion depletion and subsequent refilling were taken over a distance of more than 100 R_P. Therefore, the electromagnetic field cuboid output by AIKEF is embedded in a larger model domain for tracing the energetic heliospheric ions.

The simulation domain of the particle tracer is depicted in Figure 1. The trajectories of three sample 10 keV He^+ ions are shown to scale (solid gray/blue), compared to the size of Pluto. These ions are initialized on a "launch grid" (dashed green) upstream of the electromagnetic field cuboid from AIKEF (black), and they subsequently travel toward the region of perturbed fields near Pluto (magenta). A "detector grid" (dashed-red) is placed downstream of the dwarf planet to measure the redistribution of the energetic ion flux after these particles have passed through the interaction region. Both grids are centered on the x-axis and oriented perpendicular to the flow direction of the incident solar wind (i.e., extending in the $(\pm y)$ and $(\pm z)$ directions).

The launch grid (dashed green in Figure 1) initializes monoenergetic populations of He^+ ions with initial energy E in the rest frame of the solar wind. The extents of the grid are chosen to ensure that the initiated He^+ population includes all ions that could potentially interact with Pluto's induced magnetosphere. To evaluate this criterion, we determine the maximum distance an ion of energy E could be displaced in the y and z directions before reaching the detector grid a distance $d = u_0 P_0 = 371\ R_P$ downstream of the launch grid; the motivation for this choice of d is described later in this section. The farthest distance an ion could travel in the $(\pm y)$ direction (i.e., parallel or antiparallel to $\vec{B}_0$) before reaching the detector grid is $\Delta y_{\max} = \pm\sqrt{\frac{2E}{m}} P_0$. This distance corresponds to an ion whose initial velocity vector in the rest frame of the solar wind is oriented entirely along $\vec{B}_0$. Therefore, ions initialized on the launch grid a distance greater than $\Delta y_{\max}$ in the $(\pm y)$ direction from the AIKEF cuboid cannot interact with Pluto's induced magnetosphere before reaching the detector grid. The quantity $\Delta y_{\max}$ takes val-

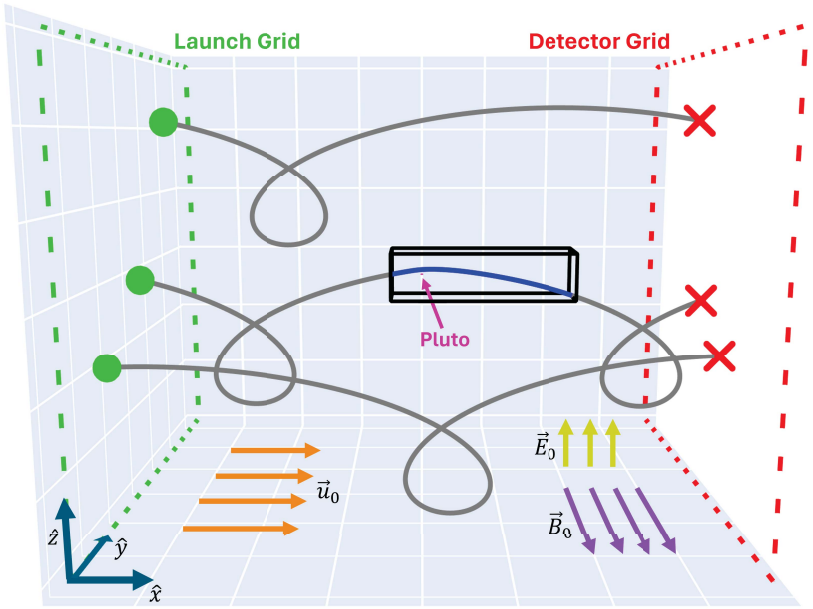

Figure 1. Diagram of the model geometry used to study energetic ion dynamics at Pluto. In this illustration, three sample 10 keV He^+ ions are launched from the upstream launch grid (indicated by dashed green lines). The electromagnetic field cuboid output by AIKEF is marked in black, within which lies Pluto (magenta). The energetic ion fluxes downstream of Pluto are measured by the detector grid (indicated by dashed red lines). The sizes of the launch and detector grids are not to scale. The green markers on the launch grid indicate where the depicted sample ions are initialized, and the red markers on the detector grid denote where they are subsequently detected. Trajectories of the three sample ions are displayed with solid lines. The line color represents which method is used to calculate their trajectory: analytical in gray outside the AIKEF cuboid where the fields are uniform (equation (7)), and numerical in blue inside the AIKEF domain where the fields are strongly draped around Pluto's ionosphere. Unit vectors $\hat{x}$, $\hat{y}$, and $\hat{z}$ denote the positive direction for each coordinate. Vectors for background quantities $\vec{u}_0$, $\vec{B}_0$, and $\vec{E}_0$ show their respective directions.

ues of 285 R_P at $E = 2$ keV and 901 R_P at $E = 20$ keV. The farthest an ion drifting in the $(+x)$ direction could be displaced from its launch point by gyration in the $(\pm z)$ direction (i.e., perpendicular to $\vec{B}_0$) is $\Delta z_{\max} = \pm 2r_g$, where r_g is the ion gyroradius. This means that ions initiated farther than $\Delta z_{\max}$ above the northern $(z > 0)$ or below the southern $(z < 0)$ extents of the AIKEF domain could not interact with Pluto's induced magnetosphere when gyrating southward or northward, respectively. The quan-

tity $\Delta z_{\max}$ varies from 91 R_P to 287 R_P across the energy range considered. The $(\pm y)$ and $(\pm z)$ extents of the AIKEF cuboid itself are each $[-32, 32]$ R_P, so the launch grid must be at least $\Delta y_{\max}$ and $\Delta z_{\max}$ farther in each respective direction. Therefore, we choose the extents of the launch grid to comfortably satisfy these conditions: $[-385, 385]$ R_P in y and $[-191, 191]$ R_P in z at $E = 2$ keV, up to $[-1001, 1001]$ R_P in y and $[-387, 387]$ R_P in z at $E = 20$ keV. A detector grid that is infinitely-extended in the $(\pm y)$ and $(\pm z)$ directions (dashed red in Figure 1) is placed downstream of Pluto, capturing the flux of all energetic ions that travel past the dwarf planet.

Outside of the AIKEF field cuboid, the electromagnetic fields are treated as uniform with the same values as the background values of the hybrid model: $\vec{B}_0 = (0, -0.24, 0)$ nT and $\vec{E}_0 = -\vec{u}_0 \times \vec{B}_0$, for $\vec{u}_0 = (403, 0, 0)$ km/s. The size of the AIKEF domain was chosen such that the fields approximately return to their background values at its outer edges (sections 2.1 and 3). The NH flyby took place at a heliocentric distance of $r = 33$ AU where the only non-vanishing component of the IMF points in the $(\pm y)$ direction, with its magnitude decreasing proportionally to $\frac{1}{r}$. Hence, the decrease in ambient magnetic field strength between the launch and detector grids would be a factor of (33 AU)/(33 AU + d), or less than 0.01%. Therefore, it is not necessary to include this decrease in our model setup. In Parker's solar wind model, the bulk velocity of the solar wind changes even more slowly with radial distance from the Sun, proportional to $\sqrt{\ln(r/r_c)}$ where r_c is the critical radius at which the solar wind becomes supersonic (Parker, 1958). Hence, the growth of the ambient flow speed between the two grids can also safely be neglected.

Energetic He^+ macroparticles are initiated at the nodes of the Cartesian launch grid, giving them initial position vectors $\vec{r}_0 = (x_0, y_0, z_0)$. In Figure 1, the depicted sample ion trajectories are initialized at the nodes highlighted by the green markers. These nodes populate the entire surface of the grid and are displaced from each other in the y and z directions by $\Delta\mathcal{Y} = \Delta\mathcal{Z} = 1.25\ R_P$. Thus, each cell of the launch grid has a size of $\Delta\mathcal{Y}\,\Delta\mathcal{Z} = 1.5625\ R_P^2$. Resolving Pluto itself with our cell size is not necessary; the actual obstacle to the solar wind is the induced magnetosphere, which is much larger than the 1.25 R_P resolution on the launch grid (Feyerabend et al., 2017; Barnes et al., 2019). This setup results in more than 189,000 nodes on the launch grid at $E = 2$ keV and nearly one million nodes on the launch grid at $E = 20$ keV. In the solar wind rest frame, energetic heliospheric ions upstream of Pluto are distributed isotropically in velocity space (McComas et al., 2017; Kollmann, Hill, McNutt, et al., 2019). Therefore,

at each node of the launch grid, the surface of a sphere in velocity space (in the rest frame of the solar wind) is populated accordingly with He^+ ions. Thus, in *Pluto's* rest frame, the initial velocity vectors of these ions at each grid node read

$$\vec{v}_0 = \begin{pmatrix} v_{x,0} \\ v_{y,0} \\ v_{z,0} \end{pmatrix} = \sqrt{\frac{2E}{m}} \begin{pmatrix} \sin\theta_v \cos\phi_v \\ \sin\theta_v \sin\phi_v \\ \cos\theta_v \end{pmatrix} + \begin{pmatrix} u_0 \\ 0 \\ 0 \end{pmatrix} \quad , \tag{1}$$

where E is the ion's observed energy in the rest frame of the solar wind, $\theta_v \in \left[\frac{\Delta\theta_v}{2}, 180° - \frac{\Delta\theta_v}{2}\right]$ is the polar angle (measured against the z-axis), and $\phi_v \in [0°, 360°)$ is the azimuthal angle (measured against the positive x-axis). The resolutions in velocity space are given by $\Delta\theta_v = 5°$ and $\Delta\phi_v = 5°$. At each node of the launch grid, the values of θ_v and ϕ_v are incremented by integer multiples of $\Delta\theta_v$ and $\Delta\phi_v$ to populate the surface of the velocity sphere in the solar wind frame. This angular resolution results in 2,592 ions being launched from each grid node. The total number of ions initialized at the launch grid is on the order of 490 million at $E = 2$ keV and 2.6 billion at $E = 20$ keV. The additional u_0 term in the first component of equation (1) is the $\vec{E} \times \vec{B}$ drift velocity associated with the convective electric field of the undisturbed solar wind.

At launch, each ion is assigned a differential intensity according to its initial energy, given by $J = \frac{1}{4\pi} I(E) \sin\theta_v \Delta\theta_v \Delta\phi_v$. In this way, the surface of the sphere we populate in velocity space represents an isotropic distribution in the rest frame of the solar wind (see also, e.g., Tippens et al., 2022; Haynes et al., 2023). The quantity $I(E)$ is the total differential intensity observable in a certain cell of the launch grid when integrating over all angles in velocity space. Figure 3 of Kollmann, Hill, Allen, et al. (2019) gives the energy spectrogram $I(E)$ of energetic He^+ ions measured by PEPSSI in two regions: one more than 200 R_P upstream of Pluto five hours before the NH encounter, and one starting at $x = 25$ R_P collected over a distance of more than 60 R_P downstream of Pluto within the energetic ion wake. These observed spectra are given in the reference frame of the spacecraft.

A comparison between the model and the observations would require transforming the observed spectra to the rest frame of the solar wind. Such a transformation would be feasible for the upstream spectrum where the solar wind is uniform, but not downstream due to the highly non-uniform solar wind flow within the region the data was collected (e.g., Feyerabend et al., 2017; Barnes et al., 2019). Therefore, instead of using the spectrograms from Kollmann, Hill, Allen, et al. (2019) to deduce the upstream differ-

ential intensity at each energy, the differential intensities of ions at each energy E are normalized such that integration over their velocity sphere yields the arbitrarily chosen value of $I(E) = 1$ cm^{-2} s^{-1} keV^{-1} sr^{-1}. Since we study the physical mechanisms leading to the depletion as well as its dependence on initial ion energy, it is suitable to investigate how an arbitrary "baseline flux" at a given energy is attenuated by Pluto's interaction region. By using the *same* value of $I(E)$ for each node of the launch grid at a given initial energy E, we assume that the observed distribution is spatially uniform across the entire upstream region (analogous to, e.g., Tippens et al., 2022; Haynes et al., 2023).

After being initialized in the rest frame of the solar wind, the differential intensity of each ion is transformed to the Pluto rest frame where the electromagnetic fields from AIKEF are provided. Equation (1) from Kollmann, Hill, McNutt, et al. (2019) gives the relation between the phase space distribution f and differential intensity J:

$$f = \frac{m}{v_{SW}^2} J_{SW} \qquad , \tag{2}$$

where m is ion mass, and the subscript "SW" indicates values for differential intensity and velocity in the rest frame of the solar wind. Since the phase space distribution f is conserved in the absence of collisions (Liouville's Theorem), we can substitute the values of J_{SW} and v_{SW} for those in the Pluto rest frame, denoted by subscript "P", and equate this new expression for f to equation (2). This yields the differential intensity in Pluto's rest frame,

$$J_P = J_{SW} \frac{E_P}{E_{SW}} \qquad , \tag{3}$$

where $E_i = mv_i^2/2$ (for $i = SW, P$) is the energy in the respective frame. An expression analogous to equation (3) is applied to obtain the differential intensity at any point along an ion's trajectory from the initial value in Pluto's rest frame.

The trajectories of energetic heliospheric He^+ ions are calculated by solving Newton's equations of motion:

$$\frac{\mathrm{d}\vec{v}}{\mathrm{d}t} = \frac{q}{m}\left[\vec{E} + \vec{v} \times \vec{B}\right] \qquad \text{and} \tag{4}$$

$$\frac{\mathrm{d}\vec{r}}{\mathrm{d}t} = \vec{v} \qquad , \tag{5}$$

where q is particle charge, and $\vec{r}$ and $\vec{v}$ are the particle's time-dependent position and velocity vectors, respectively. The method for calculating an ion's trajectory is determined by its position within the model domain. Outside of the AIKEF cuboid, where

the fields are treated as uniform, the analytical solutions for equations (4) and (5) are used (solid gray segments of the trajectories in Figure 1). For initial conditions $\vec{r}(t = 0) = \vec{r}_0$ and $\vec{v}(t = 0) = \vec{v}_0$, the analytical solution in uniform fields $\vec{B}_0$ and $\vec{E}_0$ is given by:

$$\vec{v}\,(t) = \begin{bmatrix} (v_{x,0} - u_0)\cos\Omega_0 t + v_{z,0}\sin\Omega_0 t + u_0 \\ v_{y,0} \\ -(v_{x,0} - u_0)\sin\Omega_0 t + v_{z,0}\cos\Omega_0 t \end{bmatrix} \quad \text{and} \tag{6}$$

$$\vec{r}\,(t) = \begin{bmatrix} \frac{1}{\Omega_0}(v_{x,0} - u_0)\sin\Omega_0 t - \frac{1}{\Omega_0}v_{z,0}\cos\Omega_0 t + \left[x_0 + \frac{1}{\Omega_0}v_{z,0}\right] + u_0 t \\ v_{y,0}t + y_0 \\ \frac{1}{\Omega_0}(v_{x,0} - u_0)\cos\Omega_0 t + \frac{1}{\Omega_0}v_{z,0}\sin\Omega_0 t + \left[z_0 - \frac{1}{\Omega_0}(v_{x,0} - u_0)\right] \end{bmatrix}, \tag{7}$$

where $\Omega_0 = \frac{|q||\vec{B}_0|}{m} = \frac{2\pi}{P_0}$ is the ion gyrofrequency in the uniform background field $\vec{B}_0$. Within the AIKEF cuboid, where the fields are perturbed by Pluto's interaction with the solar wind, ion trajectories must be calculated numerically (solid blue segment of the middle trajectory in Figure 1). In this region, we employ a Runge-Kutta scheme of fourth order accuracy with a timestep of $\Delta t = 2.5 \times 10^{-4}\,\Omega_0^{-1}$. Using the analytical solution in uniform fields drastically increases the computational efficiency of the model, since it allows us to propagate ions through vast regions of space without the restriction of a small timestep. This is also what allows us to use large launch grids with a small resolution of $\Delta\mathcal{Y} = \Delta\mathcal{Z} = 1.25\ R_P$. Without employing this trick, simulating energetic ion dynamics near Pluto would be infeasible.

As an example, the trajectory of the middle ion in Figure 1 is calculated analytically in uniform fields (solid gray) until it reaches the AIKEF cuboid where it is propagated numerically (solid blue). The ion subsequently exits the AIKEF cuboid at time t_a, and equations (6) and (7) are used to calculate its trajectory analytically once again. However, the initial conditions $\vec{r}_0$ and $\vec{v}_0$ appearing in these equations are updated to the position and velocity vectors the ion possesses upon exiting the AIKEF domain. By the same token, the time t in the right sides of equations (6) and (7) must be substituted with $t - t_a$ to ensure continuity in time. The small number of energetic ions whose trajectories intersect Pluto's exobase (at 1.36 R_P altitude; see Gladstone et al., 2016) are removed from the simulation. In general, the fraction of removed He^+ ions during a model run is far below 1% of the number of particles initiated on the launch grid.

2.3 Detection of Energetic Ion Fluxes

The Cartesian detector grid (dashed-red in Figure 1) is made up of cells with the *same* extensions $\Delta\mathcal{Y}$ and $\Delta\mathcal{Z}$ as the cells on the launch grid. The detector grid measures the differential flux $\mathcal{F}$ carried by ion macroparticles through each of its cells. This differential flux depends on an ion's differential intensity J and the angle between its velocity vector $\vec{v}$ and the normal of the detector plane. As the ions propagate from the launch grid through the interaction region, their energy and hence, their differential intensity will change (see equation (3)). The differential flux that an ion macroparticle carries through a cell of the detector grid is given by

$$\mathcal{F} = J\cos\alpha \qquad , \tag{8}$$

where J is the ion's differential intensity as it intersects the detector. The quantity α is the angle between the particle's velocity vector in the Pluto rest frame and the grid normal, $\hat{n} = (1, 0, 0)$, such that ions passing through the grid towards downstream (i.e., in the $+x$ direction) contribute a positive flux onto the detector.

In order to evaluate calculated maps of the flux through the detector grid, it is important to first understand that these fluxes depend on the distance d to the launch grid. To demonstrate this, Figure 2(a) illustrates the behavior of two 10 keV He^+ ions (red and blue) in uniform fields $\vec{B}_0$ and $\vec{E}_0$ over the course of a single gyroperiod P_0. The top plot shows their trajectories projected into the $y = 0$ plane. After the completion of a full gyroperiod, both ions are seen to be displaced by a distance $\Delta x = u_0 P_0 = 371$ R_P with no displacement in z. Their displacement in y, along the magnetic field direction, depends on their initial velocity component in the $(\pm y)$ direction. The bottom plot of Figure 2(a) shows the flux carried by these two macroparticles at each point along their trajectories, as it would be measured at position x by a detector grid whose normal points in the $(+x)$ direction (equation (8)). The horizontal dashed lines correspond to the initial differential flux of the respective ions when launched at the starting grid ($\Delta x = 0$, left edge of Figure 2(a)). It can be seen that only when displaced by $\Delta x = u_0 P_0$, both ions simultaneously return to the same differential flux value that they carried at launch. There are two reasons for the change in flux $\mathcal{F}$ along the ion trajectories as seen in Figure 2(a). First, the chosen detector viewing geometry plays a role: the angle α of an ion's trajectory against the $x =$ constant detector planes changes as the trajectory evolves. Second, the energy of the ions in Pluto's rest frame changes due to their $\vec{E}_0 \times \vec{B}_0$ drift,

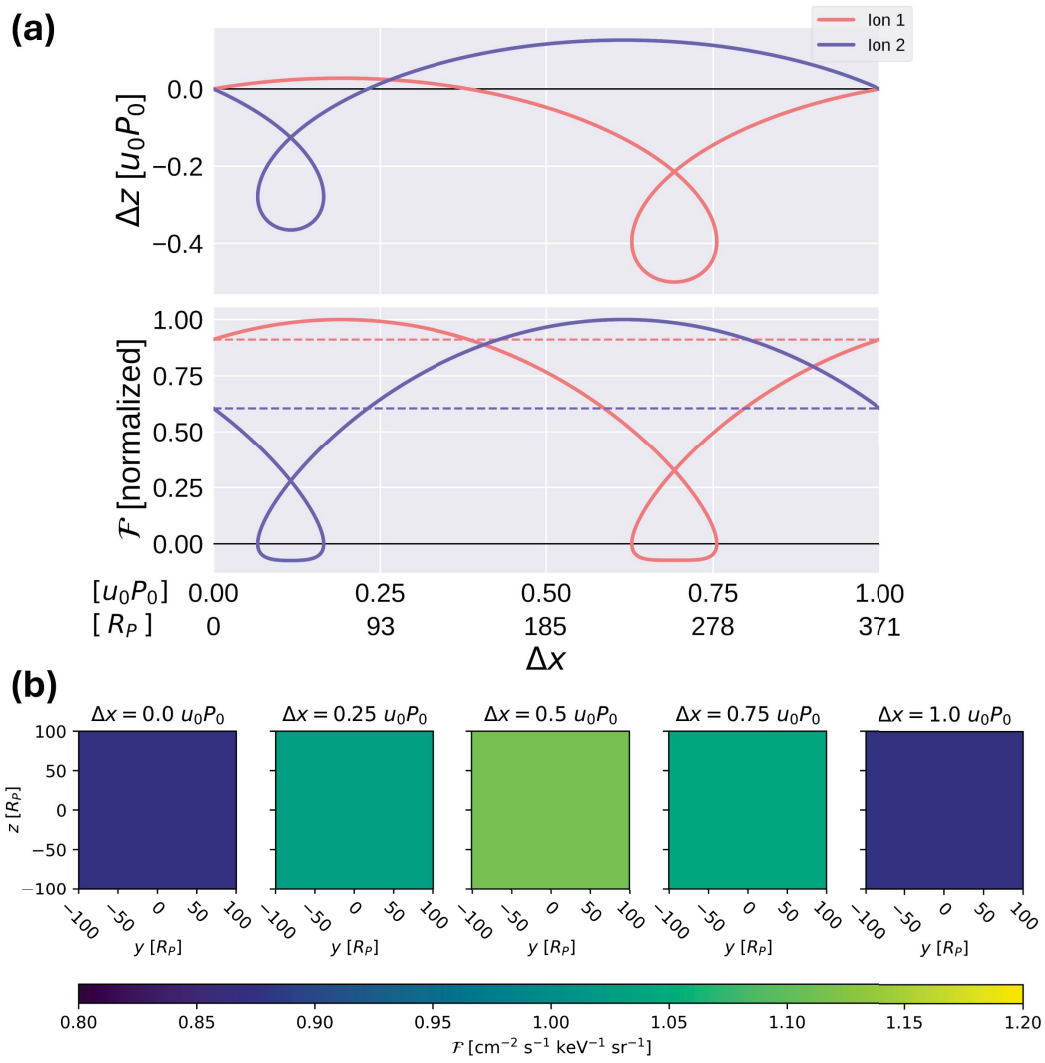

Figure 2. Panel (a) displays two sample trajectories of 10 keV He^+ macroparticles in uniform fields over a single gyroperiod P_0. The ions are launched with initial velocity vectors of $\vec{v}_0 = (1001, 179, 299)$ km/s for the red trajectory and $\vec{v}_0 = (705, 302, -544)$ km/s for the blue trajectory. The top plot illustrates the ion motion projected into the $y = 0$ plane. The axes show the ions' displacements Δx and Δz from their initial positions on the dashed-green launch grid from Figure 1 in units of $u_0 P_0$. The x-axis also has labels in units of R_P to help convey scale. The bottom plot in panel (a) shows the differential flux $\mathcal{F}(\Delta x)$ of each ion with distance Δx downstream. At each position along the ions' trajectories, we apply equation (8) to calculate the flux it carries through a (hypothetical) detector grid perpendicular to the x-axis at that position. The flux $\mathcal{F}(\Delta x)$ carried by each ion macroparticle is normalized to the maximum flux reached along its trajectory. Horizontal dashed lines indicate the differential flux carried by each ion when initialized at the launch grid. Panel (b) shows flux maps from simulations of 147 million 10 keV He^+ macroparticles in uniform fields. Just as in Figure 1, the ions are initialized on the launch grid, and their fluxes are measured at a detector grid to create the flux maps. The downstream displacement of the detector grid in each simulation with respect to the launch grid is indicated by Δx. Note that these maps are made to show the ions' behavior in uniform fields (equation (7)); therefore, neither Pluto nor the perturbed fields from AIKEF are included in this model setup.

which affects their differential intensity J (see equation (3)). Hence, even in uniform fields, the ions' gyration and drift cause a change in flux when viewed by a detector plane perpendicular to the drift direction at distances other than $\Delta x = u_0 P_0$.

The same periodic change in flux occurs when considering the "full" model setup from Figure 1. That is: initializing the surface of a velocity sphere with ion macropar-

ticles in the rest frame of the solar wind at each node on the launch grid, transforming their velocities to the Pluto rest frame, and propagating them towards the detector grid in uniform fields. Figure 2(b) shows several flux maps of He^+ ions at $E = 10$ keV in uniform fields, modeled using the setup depicted in Figure 1. The flux maps are generated by successively increasing the detector grid's distance Δx from the fixed launch grid. Hence, the $\Delta x = 0$ map corresponds to the case where the launch and detector grids coincide, so the detector grid measures the initial fluxes that the ions have at launch. Moving from left to right in Figure 2(b), each subsequent flux map increments the distance of the detector grid from the launch grid by $u_0 P_0/4$, up to a maximum of $u_0 P_0$. At each distance Δx, the recorded ion fluxes are uniform across the entire detector grid (see Figure 2(b)), since each node on the launch grid emanates the exact same ion trajectories, merely displaced in the y and z directions in increments of $\Delta\mathcal{Y}$ and $\Delta\mathcal{Z}$. The uniform flux values in the maps are seen to change from the initial value at launch ($\Delta x = 0$) as the detector grid is displaced farther in the $(+x)$ direction. After a displacement $\Delta x = u_0 P_0$, the uniform flux through the detector returns to the same value as at launch (blue in Figure 2(b)).

The periodic change in flux when moving from left to right in Figure 2(b) is a result of the $\vec{E}_0 \times \vec{B}_0$ drift in Pluto's rest frame which introduces a bias in the velocity distribution towards the positive v_x direction. Therefore, the flux measured through a detector grid depends on its distance from the launch grid. Only after a full gyroperiod, all initiated ions have drifted the same distance $\Delta x = u_0 P_0$ from the launch grid *and* each ion has returned to the same gyrophase as at launch. This periodic change in fluxes is visible in our model output because our launch grid initializes only a "slice" (at a given x position) through the energetic ion distribution approaching Pluto. Ion gyrophases change over a distance $u_0 P_0 = 371\ R_P$ in the x direction. Therefore, to cover all phases of gyration that reach the upstream face of the AIKEF domain, we would need to initialize these particles within a launch *cuboid* (i.e., an array of launch grids perpendicular to the Sun-Pluto line) extending 371 R_P along the x-axis, upstream of Pluto. In uniform fields, a detector grid would then measure the same flux at any point (x, y, z) downstream of the launch cuboid. However, implementing this approach is computationally infeasible: if the x-extent of the launch cuboid were discretized similarly to the y and z directions with a resolution of $\Delta\mathcal{X} \approx 1.25\ R_P$, runs with the highest initial energy ($E = 20$ keV) would require simulating on the order of one trillion macroparticles. However, initiat-

ing slices through the upstream distribution (using a launch grid at a given x position) does provide valuable insights into the interaction between Pluto's induced magnetosphere and the energetic ion population. Specifically, by adjusting the positions of the launch and detector grids relative to the AIKEF domain (i.e., moving the grids left or right along x in Figure 1 with constant separation d), we can trace multiple slices through the incident energetic ion population. For each position of the launch grid, the $x < 0$ face of the AIKEF cuboid is met with different gyrophases of impinging ions. Thus, by considering the downstream flux maps for different positions of the launch grid, this approach allows us to probe the 3D structure of the region where the energetic ion flux is attenuated by Pluto.

In conclusion, by keeping the launch and detector grids a distance $d = u_0 P_0$ (or any integer multiple of d) apart, we ensure that the flux measured in uniform fields is identical to the flux that we initialize at the launch grid (Figure 2(b)). For other distances between the two grids, the flux through the detector is attenuated or enhanced—even in perfectly uniform fields—merely by the distribution being observed at different phases. In this case, a reduction or enhancement in flux measured by the detector grid relative to the flux at the launch grid is not necessarily caused by the interaction between these particles and Pluto's induced magnetosphere. At each initial He^+ energy E, multiple simulations are run varying the x-positions of the two grids with respect to Pluto while keeping the displacement d between them the same. Starting with the detector grid placed at $x = 25\ R_P$ downstream of Pluto, we increment its distance from the dwarf planet in units of $u_0 P_0/8 \approx 46\ R_P$ up to a maximum of $u_0 P_0/2$ (at $x \approx 210\ R_P$). This range of detector grid positions encompasses the estimated $x = 190\ R_P$ extent of the energetic ion wake (Kollmann, Hill, Allen, et al., 2019).

For each run, our tracing tool calculates the trajectories of a single set of sample macroparticles, i.e., the "slice", that we initiate on the launch grid at time $t = 0$. However, in reality there would be a continuous inflow of ions from the nodes of the launch grid toward downstream. This inflow would populate each physical trajectory with an ion at every point at any given time. Thus, our model identifies the pathways in phase space that connect the launch grid to the detector grid and takes a snapshot of the ions populating these paths at the position of the detector. To illustrate this, Figure 3 depicts the trajectory of a 10 keV He^+ ion (purple). It intersects the launch grid (vertical black line, left) at three points a, b, and c. If we consider the depicted trajectory to

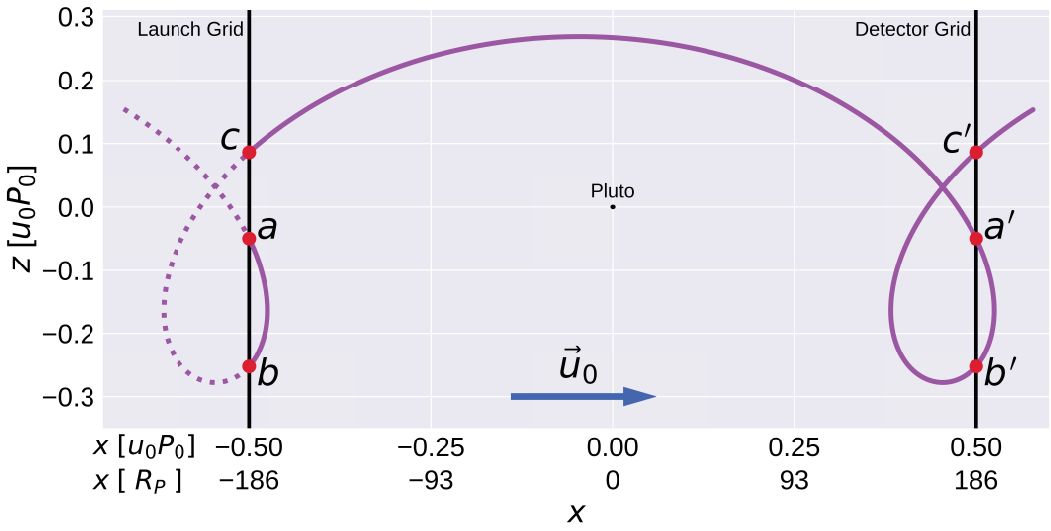

Figure 3. Plot of a sample 10 keV He^+ trajectory in uniform fields (purple; given by equation (7)) lying in the $y = 0$ plane as it intersects the launch (left vertical line) and detector (right vertical line) grids. Points a, b, and c mark the trajectory's intersections with the launch grid, while points a', b', and c' mark its intersections with the detector grid. The solid segments of the trajectory indicate where this sample ion would be "allowed" to travel. The dotted segments indicate portions of the trajectory where this ion could not travel, since it would be deleted as it passes through the launch grid from downstream to upstream. In our model, the launch and detector grids are kept a distance u_0P_0 apart: primed and unprimed points of the same letter are exactly one gyroperiod apart in time, and u_0P_0 apart in x. Pluto is marked by the small black circle at the origin for size reference; its effect on the fields is not considered for this trajectory.

be populated by a sample ion at each point (as it would be in reality), we see that ions launched from the grid node at point a would contribute to the distributions initiated at grid nodes b and c of the launch grid. However, an ion with the same phase space coordinates is already being initialized in the velocity spheres at points b and c (see equation (6)). In order to avoid misrepresenting the initial flux at points b and c, our tracing model (Figure 1) deletes all ions that would pass through the launch grid from downstream to upstream (i.e., with a negative v_x component). With this approach, the ions launched on the grid nodes at points a and b following the depicted trajectory would inevitably be deleted: the ion from a is deleted upon returning to the launch grid, and the ion from b is removed from the model right after being initialized. However, the ion initiated at point c would continue propagating towards the detector grid. This approach

to launching ions is identical to the method used in AIKEF to generate, and continuously replenish, the Maxwellian upstream distribution of the solar wind at the left face ($x = -20\ R_P$) of the hybrid model domain (Müller et al., 2011).

Our model emulates a *continuous* flow of ions from the launch grid toward the detector. Therefore, at any given time, each point along a trajectory (i.e., an "allowed" path through phase space) is assumed to be populated by an ion macroparticle. This means that at a given point in time, the depicted trajectory in Figure 3 simultaneously contributes to the flux through the detector at three distinct points (a', b', and c'), corresponding to the intersections between the detector grid and the trajectory of the ion launched from point c. This method of detection and the treatment of the launch grid described above have been applied to generate the flux maps in Figure 2(b).

3 Model Results

3.1 Hybrid Simulation of Pluto's Induced Magnetosphere

Figure 4 depicts snapshots of the quasi-stationary electromagnetic fields output by the AIKEF hybrid model (section 2.1). The magnitudes of the electric field $|\vec{E}|$ and magnetic field $|\vec{B}|$ are plotted as colormaps spanning the extent of the AIKEF domain in the $y = 0$ (left column) and $z = 0$ (right column) planes. Panels 4(a) and 4(b) show $|\vec{B}|$, while panels 4(c) and 4(d) depict $|\vec{E}|$. The structure of Pluto's interaction region at the time of the NH flyby, as revealed by hybrid models, has already been discussed in detail by Feyerabend et al. (2017) and Barnes et al. (2019). Therefore, we restrict our discussion to those features that are most apposite to our subsequent analysis of energetic ion dynamics (section 3.2).

An induced magnetosphere is formed around Pluto, indicated by the regions of perturbed fields in Figure 4. The bow shock is located 4-5 R_P upstream of the dwarf planet's center, consistent with the value of 4.5 R_P determined by McComas et al. (2016) from SWAP observations. Inside the bow shock and immediately upstream of Pluto is the magnetic pileup region that stems from the deceleration of the impinging solar wind (panels 4(a) and 4(b)). The magnetic field magnitude above Pluto's ramside hemisphere reaches a peak strength of over eight times the background value $|\vec{B}_0|$. Panels 4(b) and 4(d) illustrate that Pluto's induced magnetosphere is symmetric in the $z = 0$ plane (containing $\vec{B}_0$) within which the magnetic draping pattern is most pronounced. Pluto's mag-

netotail gradually increases in width with distance from the dwarf planet. The magnetic field strength drops below $|\vec{B}_0|$ in the thin neutral sheet separating the two lobes (dark blue "ray" along $y = 0$ in Figure 4(b)).

Figures 4(a) and 4(c) illustrate the asymmetry of Pluto's induced magnetotail in the $y = 0$ plane (i.e., perpendicular to $\vec{B}_0$), caused by the large gyroradii of ionospheric pickup ions. The most dense part of the heavy ion tail coincides with the region of near-zero electric field strength extending slightly south of $z = 0$ (see panel 4(c) and Feyerabend et al., 2017). Plutogenic pickup ions are accelerated along the direction of the convective electric field to form the thin, disk-like pickup tail that extends several 100 R_P northward, following the initial segment of the ions' gyration. The motion of these ions and the formation of the pickup tail are also illustrated in Figure 6 of Barnes et al. (2019). The pickup tail is largely confined to the neutral region between the two magnetotail lobes (seen in panels 4(b) and 4(d)), consistent with the results illustrated in Figure 10 of Barnes et al. (2019) for an IMF strength near 0.24 nT. To conserve the total momentum of the impinging plasma as the Plutogenic ions stream northward, the solar wind is deflected southward while continuing to travel toward downstream; this can be seen in Figure 4(a) of Feyerabend et al. (2017). The deflection of the solar wind in the southern hemisphere stretches the magnetic pileup region dozens of R_P toward downstream along the southern flank of the pickup tail (see our Figure 4(a)). Along this flank, $|\vec{E}|$ and $|\vec{B}|$ both increase up to four times their background values.

Figure 5 plots $|\vec{E}|$ and $|\vec{B}|$ in cross-sections of Pluto's magnetotail perpendicular to the x-axis. The region of elevated field strength within the magnetotail retains a roughly circular shape with a radius that increases from 15 R_P at $x = 25$ R_P to more than 25 R_P at $x = 100$ R_P. The southern edge of the magnetotail is defined by the magnetic pileup region that is stretched along its flank (dark red arc in the $|\vec{B}|$ plot at $x = 25$ R_P, yellow-green arc in the $|\vec{E}|$ plot at $x = 25$ R_P). The neutral region between the two magnetic lobes (dark blue "ray" along $y = 0$ in all eight panels) possesses a pronounced north-south asymmetry. In the $z > 0$ half-space, it continues through the $z = 32$ R_P face of the AIKEF domain. In the south, it reaches no farther than the arc of elevated field strength from the deflected solar wind. This asymmetry is associated with the initial direction of the Plutogenic pickup ions' gyration: northward along the convective electric field. Similar asymmetries in the fields are also found at, e.g., Titan, active comets, or during the AMPTE experiment where pickup ion gyroradii are likewise

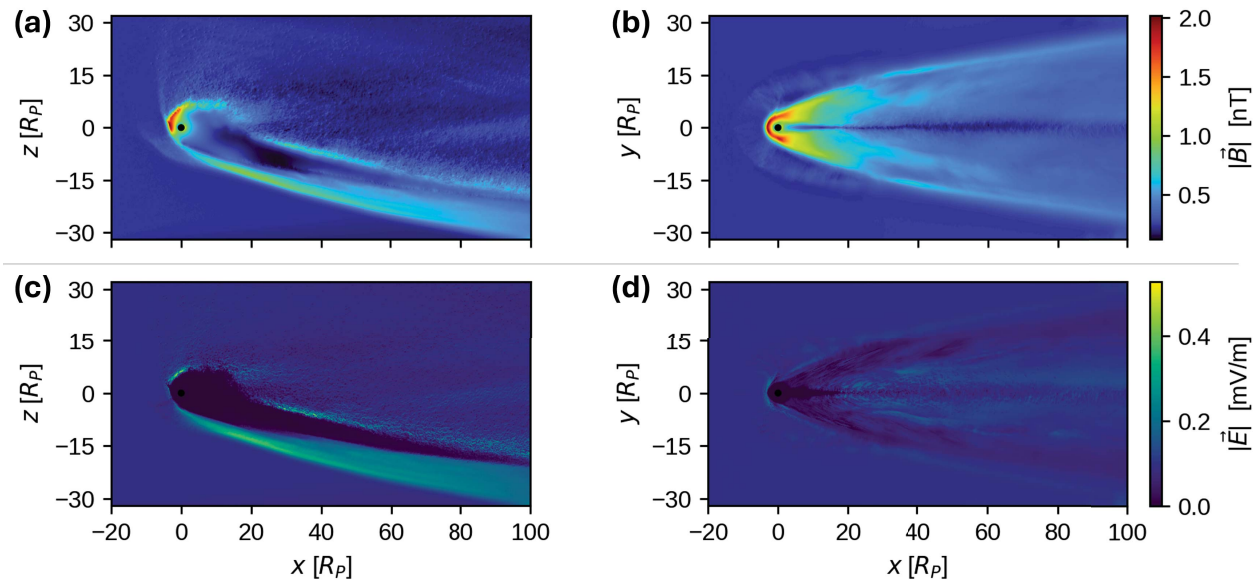

Figure 4. Electric and magnetic field magnitude near Pluto, as output by the AIKEF hybrid model. Panels (a) and (b) depict $|\vec{B}|$, while panels (c) and (d) show $|\vec{E}|$. Field magnitudes in the $y = 0$ and $z = 0$ planes are in the left and right columns, respectively. Pluto is denoted by the solid black circle at the origin.

large relative to the size of the obstacle in the plasma flow (Delamere et al., 1999; Simon et al., 2007; Regoli et al., 2016; Nilsson et al., 2017).

3.2 Energetic Ion Tracing

Figure 6 depicts output from four different runs of the energetic He^+ tracing model (section 2.2). In each run, a monoenergetic ion population is launched, with initial energies from $E = 2$ keV up to $E = 20$ keV. In all model setups, the launch grid is located at $x = -346\ R_P$ such that the detector grid, displaced $d = u_0 P_0$ toward downstream, is positioned at $x = 25\ R_P$. The detector grid is located where the depletion in He^+ flux observed by PEPSSI was strongest (Kollmann, Hill, Allen, et al., 2019). The maps sum the flux $\mathcal{F}$ carried by He^+ macroparticles through each cell of the detector plane. The colorscale measures the deviation in flux from the value $\mathcal{F}_0$ at each energy E in uniform fields.

The maps of Figure 6 each exhibit a region of decreased flux in the north ($z > 0$) and a region of elevated flux in the south ($z < 0$). The maximum magnitude of the de-

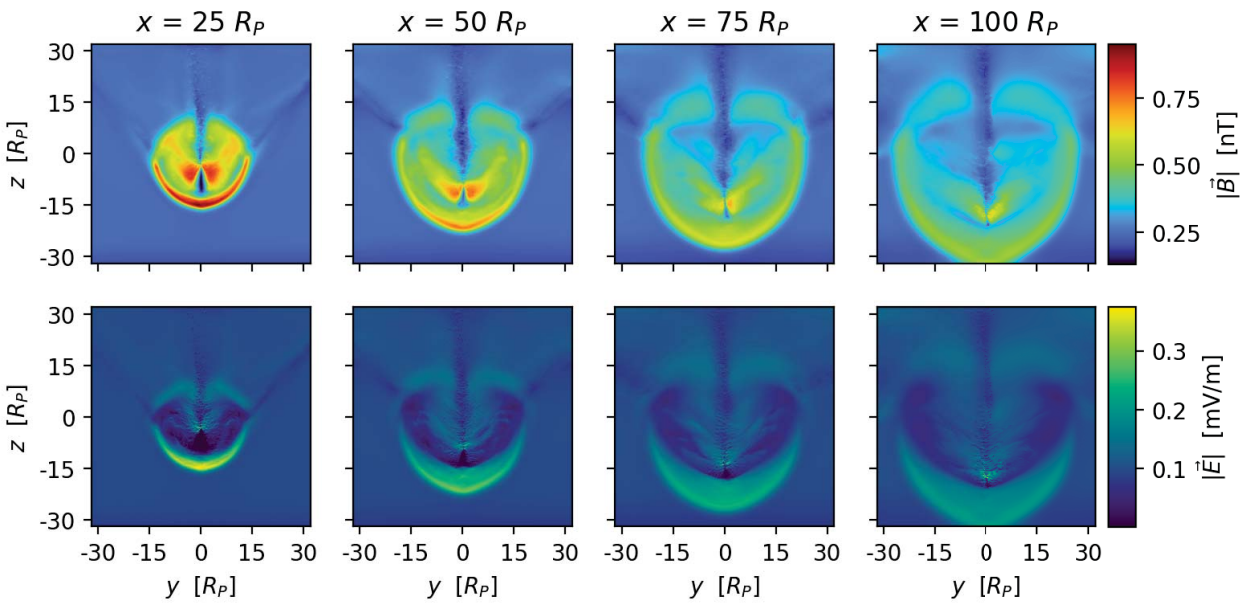

Figure 5. Electric and magnetic field magnitude in cross-sections of Pluto's magnetotail perpendicular to the Sun-Pluto line, as output by the AIKEF hybrid model. The top row of plots depicts $|\vec{B}|$, while the bottom row depicts $|\vec{E}|$. Each column shows the fields in the x = constant cutting plane indicated above. The colorscales used in these plots do not align with those in Figure 4 in order to highlight fine structures in the magnetotail. Note that Pluto itself is not intersected by any of these cutting planes.

viation between $\mathcal{F}$ and $\mathcal{F}_0$ decreases from 41% in the $E = 2$ keV map to 12% in the $E = 20$ keV map. By $E = 100$ keV (not depicted), the greatest perturbation in flux is merely a decrease from $\mathcal{F}_0$ by 9%. In other words, higher energy ions experience less deflection. For the $E = 2$ keV run, the non-uniformities in flux are largely confined to two crescent-shaped regions centered on $y = 0$ (left panel in Figure 6). Only a few R_P northward of Pluto's equatorial plane ($z = 0$) is a crescent of decreased flux (dark blue). This structure is more than 25 R_P wide, has a north-south extent (i.e., "height") of about 10 R_P, and exhibits a reduction in flux by approximately 41%. The crescent of elevated flux (red) in the south ($z < 0$) has a similar height and extent in the $\pm y$ direction as the depletion in the north. The magnitude of this enhancement in flux is comparable to the northern depletion. The shape, extent, and magnitude of the enhancement and depletion features evolve with increasing initial energy (see Figure 6). At an initial energy of $E = 5$ keV, the width of the southern crescent has decreased to about 24 R_P, but

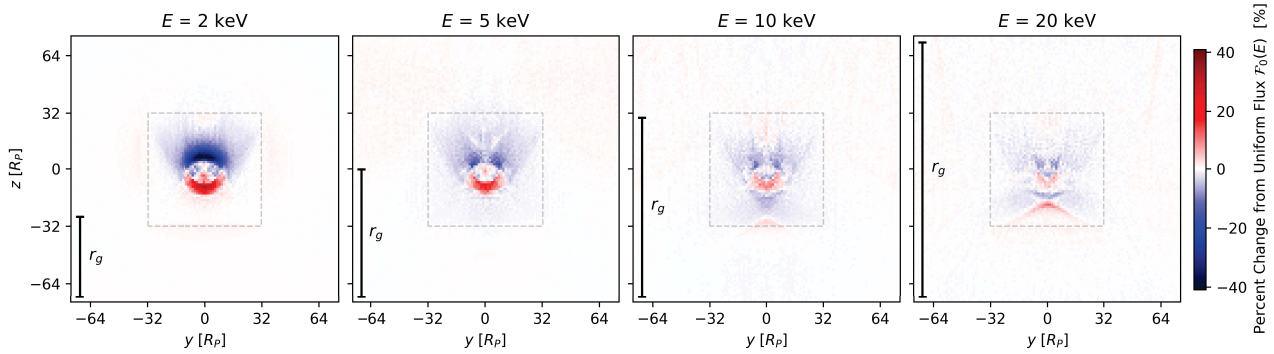

Figure 6. Output of the energetic particle tracer (section 2.2) for He^+ ions, initiated at the launch grid with starting energies E of 2, 5, 10, and 20 keV (from left to right). In each of the four model runs, the detector grid is placed at $x = 25\ R_P$, and the launch grid is a distance $d = u_0 P_0$ upstream of the detector at about $x = -346\ R_P$. The extent of the AIKEF cuboid perpendicular to the x-axis is indicated by the dashed gray lines. The colorscale describes the deviation in differential flux from what would be measured in uniform fields for the same grid geometry: $100\% \cdot (\mathcal{F} - \mathcal{F}_0(E))/\mathcal{F}_0(E)$. Here, $\mathcal{F}$ represents the total flux carried by macroparticles into each cell of the detector grid in perturbed fields, and $\mathcal{F}_0(E)$ denotes the corresponding value in uniform fields. In each map, the vertical bar illustrates the length of the gyroradius of an He^+ ion whose initial velocity vector is perpendicular to $\vec{B}_0$. Thus, this bar represents the maximum gyroradius that these ions can have at each initial energy.

it maintains a similar extension in the north-south direction than at $E = 2$ keV. By $E = 20$ keV, the elevated flux has been redistributed into a more complex pattern while still confined to the south (right panel of Figure 6). This northern-depletion, southern-enhancement flux pattern persists for initial energies E up to 100 keV.

To understand this north-south dichotomy in the He^+ fluxes downstream of Pluto, Figures 7(a)–(d) display the trajectories of several sample He^+ macroparticles with initial energy $E = 2$ keV as they travel through the AIKEF domain. The upper plot in each panel depicts an ion's trajectory through Pluto's induced magnetosphere (solid gray). It is accompanied by a second ion trajectory (dashed gray) with identical initial conditions, propagating through *uniform* fields $\vec{E}_0$ and $\vec{B}_0$ to illustrate the effect of the draped fields on the first ion. The vertical black line in each plot at $x = 25\ R_P$ indicates the location of the detector grid from Figure 6. To contextualize how the perturbed fields

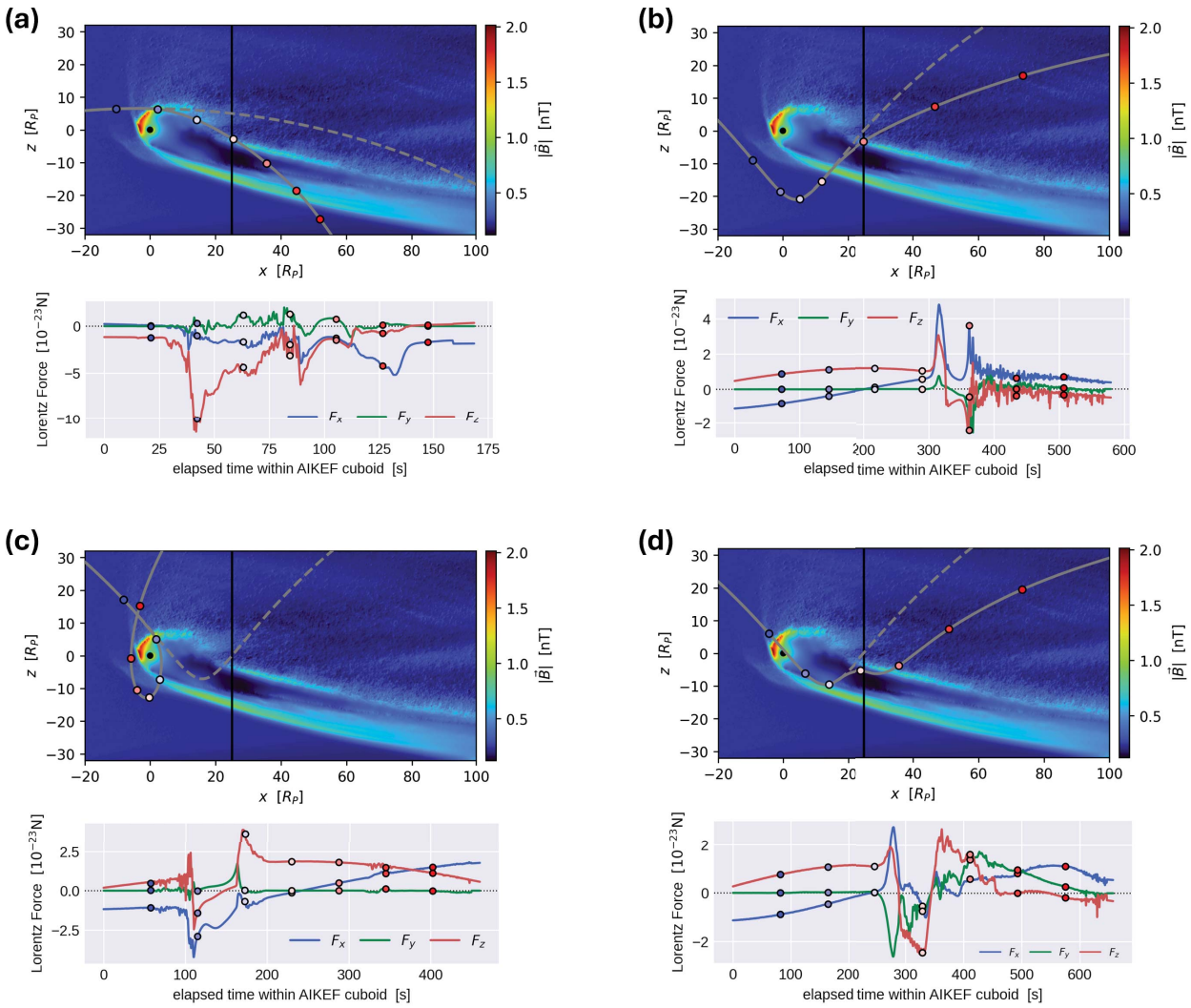

Figure 7. Examples of energetic ion dynamics at Pluto in uniform and draped fields. The top plot in panels (a)–(d) depicts a sample He^+ macroparticle's trajectory (solid gray; initial energy $E = 2$ keV) through the perturbed fields from AIKEF near Pluto (black circle), projected into the $y = 0$ plane. In each case, the trajectory that a macroparticle with the same initial conditions would follow in uniform fields is also shown (dashed gray). These ion trajectories are among those that contribute to the $E = 2$ keV flux map of Figure 6, i.e., they are initialized on the launch grid at $x = -346\ R_P$, a distance $d = u_0 P_0$ upstream of the detector grid (vertical black line) at $x = 25\ R_P$. The bottom plot in each panel depicts the three components of the Lorentz force $\vec{F}_L$ experienced by the ion while traveling through the AIKEF cuboid (i.e., along the solid gray trajectory). The colored, circular markers in the upper and lower plots of each panel correspond to the same points in time. The macroparticle trajectories are overlaid on top of colormaps of the magnetic field magnitude $|\vec{B}|$ in the $y = 0$ plane. The initial conditions for the depicted ions are: $\vec{r}_0 = (-345.9, 0, 5.0)\ R_P$ and $\vec{v}_0 = (701.9, 0, -80.1)$ km/s for panel (a); $\vec{r}_0 = (-345.9, 0, 0)\ R_P$ and $\vec{v}_0 = (236.7, 0, 261.0)$ km/s for panel (b); $\vec{r}_0 = (-345.9, 0, 0)\ R_P$ and $\vec{v}_0 = (142.0, 0, 166.3)$ km/s for panel (c); and $\vec{r}_0 = (-345.9, 62.5, 0)\ R_P$ and $\vec{v}_0 = (165.8, -63.5, 188.4)$ km/s for panel (d).

in the AIKEF domain modify the trajectory, the lower plots in Figures 7(a)–(d) display the components of the Lorentz force $\vec{F}_L = q\left(\vec{E} + \vec{v} \times \vec{B}\right)$ acting upon the ion in perturbed fields. Because the maximum gyration speed ($\sqrt{\frac{2E}{m}} \sin\psi = 310$ km/s for a pitch angle of $\psi = 90°$) of a He^+ ion at $E = 2$ keV is smaller than the speed of the $\vec{E}_0 \times \vec{B}_0$ drift ($u_0 = 403$ km/s), it will never have a negative v_x component in uniform fields. Thus,

in contrast to the examples from Figures 1–3, consecutive arcs of its trajectory do not overlap; this is true for He^+ ions with initial energies less than $E = 3.39$ keV. The segments of the ions' trajectories spanned by the first four time markers (colored circles) of panel 7(b) illustrate their motion along a curtate cycloid in the uniform fields upstream of Pluto.

Figure 7(a) shows the trajectory of a He^+ ion with an initial gyrophase such that it approaches the magnetic pileup region near the "top" of a cycloidal arc where v_x is close to its maximum and v_z is nearly zero. This ion and its companion in uniform fields are initialized on the launch grid in the $y = 0$ plane with zero velocity along $\vec{B}_0$. Therefore, they both remain in this plane before reaching the AIKEF domain. In perturbed fields, the ion enters the induced magnetosphere between the first and second time markers (dark and light blue circles) and intersects the upstream pileup region of maximum field strength slightly north of Pluto at the second marker. Due to the field enhancement, the ion's gyroradius r_g locally decreases from 45 R_P to about 8 R_P. This sharp drop in gyroradius in conjunction with the ion's clockwise gyration causes its trajectory to be diverted southward when moving downstream. This deflection is also visible in the illustration of the Lorentz force (lower plot of Figure 7(a)): starting around the second time marker, the (negative) $F_{L,z}$ component dominates by up to a factor of six. In draped fields, the ion intersects the detector south of $z = 0$. However, in uniform fields (dashed line), this sample ion would deposit its flux onto the detector grid slightly north of Pluto's equatorial plane.

Similarly, the sample He^+ ion in panel 7(c) enters the AIKEF domain near its top left corner within the $y = 0$ plane. However, this particle approaches the magnetic pileup region with a negative v_z component, at a steeper angle than the sample ion from panel 7(a). Immediately prior to the second time marker (light blue circle), the ion's trajectory is initially deflected southward relative to the trajectory in uniform fields; this is indicated by the dips in $F_{L,x}$ and $F_{L,z}$ near the second marker in the plot of the Lorentz force. Between the second and third time markers, the ion travels through the region of near-zero electric field within the heavy ion tail (dark blue in Figure 4(c)), i.e., its $\vec{E}\times\vec{B}$ drift nearly ceases, allowing it to gyrate northward and back toward upstream. This is why the trajectory in perturbed fields ultimately intersects the detector plane *north* of the trajectory in uniform fields. Since this ion impinges onto the detector grid far out-

side the bounds of the AIKEF domain (dashed lines in Figure 6), it ultimately contributes to a reduction in flux near Pluto's downstream equatorial plane.

The sample 2 keV He^+ ion in Figure 7(b) again enters the AIKEF domain at the $x = -20\ R_P$ face with initial conditions that confine its trajectory upstream of Pluto to the $y = 0$ plane. However, it approaches the perturbed fields with a different incoming gyrophase than the sample particles from panels 7(a) and (c). The ion enters the stretched pileup region along the southern flank of the pickup tail, encountering it from "below" with a positive v_z component between the fourth and fifth time markers (light pink and pink markers). The elevated field strength causes the ion to be deflected southward relative to the trajectory in uniform fields, again as a result of the localized decrease in gyroradius. This deflection is indicated by the seven times increase in $F_{L,x}$ immediately following the fourth marker; the positive $F_{L,x}$ component of the Lorentz force serves to "level off" the ion's trajectory through acceleration towards downstream. Thus, despite the simultaneous increase in $F_{L,z}$ by a factor of three, the greater increase in $F_{L,x}$ causes the ion to remain to the south of the trajectory in uniform fields. Closer to the fifth marker (pink), $F_{L,z}$ ultimately becomes negative, thereby pushing the ion further southward.

In panel 7(d), the sample He^+ ion is initialized on the launch grid with $E = 2$ keV, but *outside* of the $y = 0\ R_P$ plane at $y = 62.5\ R_P$. This ion initially possesses a negative $v_{y,0}$ component such that it approaches Pluto's induced magnetosphere from the $y > 0$ half-space. The ion begins to diverge from the trajectory in uniform fields between the third and fourth time markers (pale blue and light pink circles), indicating its passage through the stretched pileup region along the southern flank of the pickup tail (see Figure 5). The ion's southward deflection is facilitated by the spike in $F_{L,x}$ that "levels off" the trajectory and the drop in $F_{L,z}$ to negative values between the third and fourth time markers. The deviation of the trajectories in uniform and draped fields illustrates that the southward deflection is not unique to ions that impinge from within the $y = 0$ plane (e.g., panels 7(a)–(c)) or directly onto the ramside magnetic pileup region (e.g., panels 7(a) and 7(c)). The southward deflection experienced by the ions in Figures 7(a)–(d) manifests in the $E = 2$ keV flux map of Figure 6 as the regions of decreased flux in the north and elevated flux in the south. We note that the locations of these features depend entirely on the IMF orientation: if $\vec{B}_0$ pointed in the $(+y)$ direction instead (in contrast to the conclusions of Zirnstein et al. (2016)), the regions of enhanced or depleted flux from Figure 6 would be mirrored across the $z = 0$ plane.

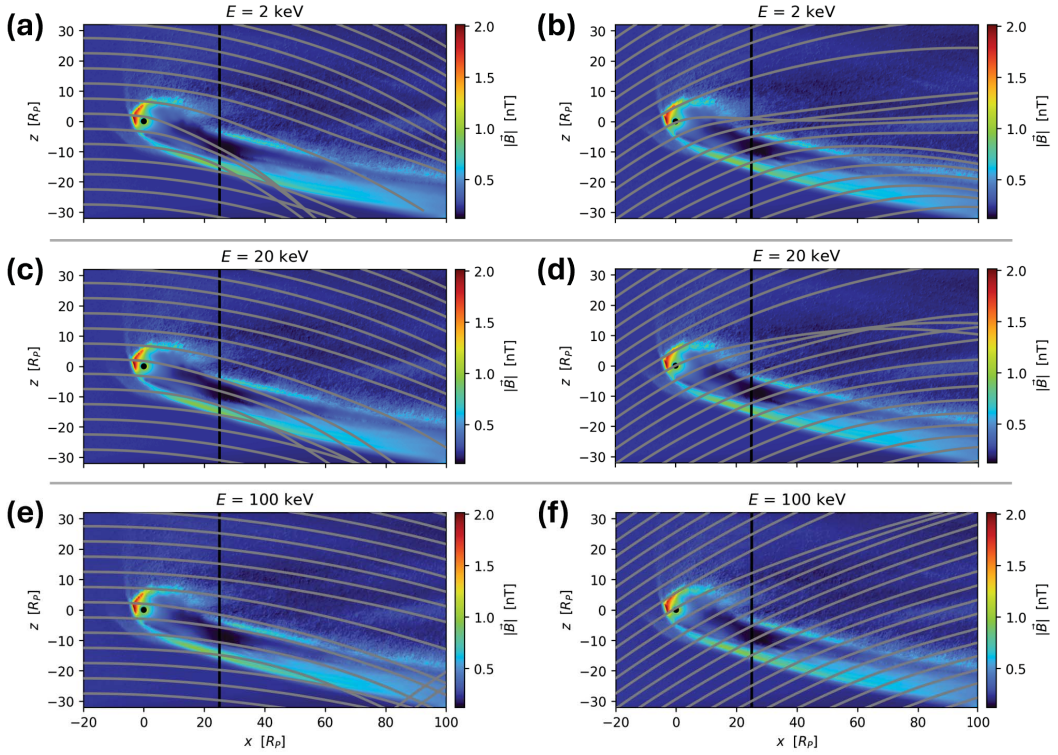

Figure 8. Trajectories (gray) of multiple sets of He^+ ions in perturbed fields near Pluto at three initial energies, projected into the $y = 0$ plane: $E = 2$ keV in panels (a) and (b), $E = 20$ keV in panels (c) and (d), and $E = 100$ keV in panels (e) and (f). An array of ions is initialized in each panel at the left edge of the AIKEF domain ($x = -20\ R_P$). Their initial positions lie in the $y = -3\ R_P$ plane such that their trajectories do not intersect Pluto (black circle). In panels (a), (c), and (e), the ions are launched from $z = -32.5\ R_P$ to $z = 57.5\ R_P$ in increments of $\Delta z = 5\ R_P$. For each initial energy E, these ions are initiated with the same starting velocity of $\vec{v}_0 = \left(\sqrt{2E/m} + u_0, 0, 0\right)$ such that they impinge upon the induced magnetosphere with only a slight southward incline ($v_z < 0$) against the x-axis. In panels (b), (d), and (f), the ions are launched from $z = -102.5\ R_P$ to $z = 37.5\ R_P$, again in increments of $\Delta z = 5\ R_P$. These ions also have initial velocity vectors with a 90° pitch angle (i.e., $v_{y,0} = 0$), however, they are inclined by 35° northward against the x-axis and enter Pluto's interaction region with a positive v_z component. To provide context, the colormap illustrates the magnetic field magnitude $|\vec{B}|$ from AIKEF in the $y = 0$ plane. The intersection between the depicted plane and the detector grid from Figure 6 is indicated by the vertical black line at $x = 25\ R_P$. The trajectory that appears to abruptly "end" near the bottom right corner of panel (a) exits through the face of the AIKEF domain at $y = -32\ R_P$, after which the ion's path is no longer plotted. The trajectory segments that apparently "emanate" from the lower edge of the AIKEF domain in panel (e) represent ions that initially exit and then return. At an initial energy of $E = 100$ keV, the speed of ion gyration is much larger than their drift speed, so these ions are capable of re-entering the northward portion of their gyromotion before drifting downstream the length of the AIKEF domain.

As initial ion energy E increases across the flux maps in Figure 6—and to higher energies up to $E = 100$ keV—there is a gradual decrease in the magnitude of the flux perturbations recorded by the detector grid. The reason for this is elucidated in Figure 8 which depicts multiple sets of sample He^+ macroparticle trajectories (gray) through Pluto's induced magnetosphere at three initial energies: $E = 2$ keV (panels 8(a) and 8(b)), $E = 20$ keV (panels 8(c) and 8(d)), and $E = 100$ keV (panels 8(e) and 8(f)). These energies cover the range measured by the PEPSSI instrument during the flyby of Pluto (Kollmann, Hill, Allen, et al., 2019). The maximum gyroradii for these energies are 45 R_P, 143 R_P, and 321 R_P, respectively. At each energy, the set of ions is initial-

ized along a line parallel to the z-axis within the left face of the AIKEF domain ($x = -20\ R_P$) at $y = -3\ R_P$. For the purpose of this figure, we do *not* initialize these sample ions at $y = 0$ such that they avoid impacting Pluto or interacting with its neutral atmosphere. This is done to illustrate that the contribution these ions make to the flux patterns on the detector grid (vertical black line at $x = 25\ R_P$) are solely due to the induced magnetosphere, and not to absorption by Pluto or its atmosphere. The trajectories are overlaid on a colormap of $|\vec{B}|$ in the $y = 0$ plane to provide context for the field geometry. The launch points of the ions in the left column (panels 7(a), (c), and (e)) are located between $z = -32.5\ R_P$ and $z = 57.5\ R_P$, displaced in increments of $\Delta z = 5\ R_P$. At each energy, the ions have the same initial velocity of $\vec{v}_0 = \left(\sqrt{2E/m} + u_0, 0, 0\right)$ such that they approach the perturbed fields near the "top" of their trajectories (similar to the ion in Figure 7(a)). In the right column (panels 8(b), (d), and (f)), the ions have starting velocity vectors that are initially inclined by 35° northward against the x-axis, such that they impinge upon the perturbed fields with a positive v_z component (similar to the ion in Figure 7(b)). To facilitate these ions' interaction with Pluto's induced magnetosphere, the range of their launch points is displaced southward compared to the left column of Figure 8: they span from $z = -102.5\ R_P$ to $z = 37.5\ R_P$, again separated by increments of $\Delta z = 5\ R_P$. Thus, the columns of Figure 8 compare particles that possess *different* gyrophases when approaching Pluto's induced magnetosphere.

In panel 8(a), the $E = 2$ keV macroparticles launched close to Pluto's equatorial plane (between $z = -7.5\ R_P$ and $z = 2.5\ R_P$) are seen to be heavily deflected southward; the same is true for the ions emanating from $z = -12.5\ R_P$ and $z = -17.5\ R_P$ in panel 8(b). This leaves a gap of more than 10 R_P in z direction between adjacent ion intersections with the detector grid, and causes an accumulation of the macroparticle trajectories south of the gap. At $E = 20$ keV (panels 8(c) and (d)), the gap between adjacent particle impacts onto the detector grid has decreased in z extent to less than 10 R_P. Nonetheless, the deflected ions are still "focused" south of the gap. This can be seen in the $z \in [-10, -15]\ R_P$ segment of the detector grid in panel 8(c) and the $z \in [0, 10]\ R_P$ segment in panel 8(d). By $E = 100$ keV (panels 8(e) and (f)), the trajectories passing the detector grid are seen to be only slightly perturbed, and any gaps form farther downstream. For larger initial energy, the segments of the ions' trajectories within the regions where the field perturbations are strongest become increasingly small relative to the scale of their gyromotion. Hence, the "ability" of Pluto's induced magnetosphere to

modify the ion trajectories is diminished. Thus, the flux maps in Figure 6 exhibit a decrease in the magnitude of the perturbations recorded by the detector grid as initial ion energy E increases.

Figure 9 depicts flux maps, calculated for He^+ at an initial energy of $E = 2$ keV using five different locations of the launch grid and associated detector grid. The top plot illustrates the positions of the grids used in each of the five runs. The colored vertical lines at the left side represent the positions of the launch grids, whereas those at the right correspond to the positions of the respective detector grids $d = u_0 P_0 = 371\ R_P$ farther downstream. The detector grid closest to Pluto (red) is at $x = 25\ R_P$; the succeeding detectors are displaced downstream in increments of $u_0 P_0/8 \approx 46\ R_P$ to a maximum of $x = 210\ R_P$ (purple). Only the two detectors that are closest to Pluto at $x = 25\ R_P$ (red) and $x = 71\ R_P$ (yellow) intersect the AIKEF domain, whereas the others do not. The bottom row of Figure 9 depicts maps of the He^+ flux measured by the detector grids in these five runs of the energetic ion tracer. Analogous to Figure 6, red values on the color bar indicate an increase in flux and blue values denote a decrease in flux relative to the value in uniform fields $\mathcal{F}_0$.

The leftmost flux map at $x = 25\ R_P$ (red border) is identical to the $E = 2$ keV map of Figure 6, displaying the double-crescent pattern of reduced flux in the north and elevated flux in the south. For the detector grid at $x = 71\ R_P$ (orange border), the morphology of the observed flux pattern is still similar, however, both the enhancement and depletion have increased in area by more than a factor of two compared to the $x = 25\ R_P$ case. Because the detector at $x = 71\ R_P$ is farther downstream, the trajectories of ions deflected near Pluto are spread across a larger area: this is visible in the $(\pm z)$ direction in Figures 8(a) and 8(b). Additionally, a "corona" of slightly elevated He^+ flux is seen to surround the two prominent regions of increased and decreased flux in the $x = 71\ R_P$ map. This "corona" persists and increases in area with farther distance to Pluto out to $x = 210\ R_P$; it is constituted by ions that experience significant deflection in the $(\pm y)$ directions as they encounter the draped fields. Figure 7(d) depicts an example of such a trajectory that is deflected in the $(-y)$ direction as it encounters Pluto's induced magnetosphere, indicated by the negative spike in $F_{L,y}$ following the third time marker (pale blue).

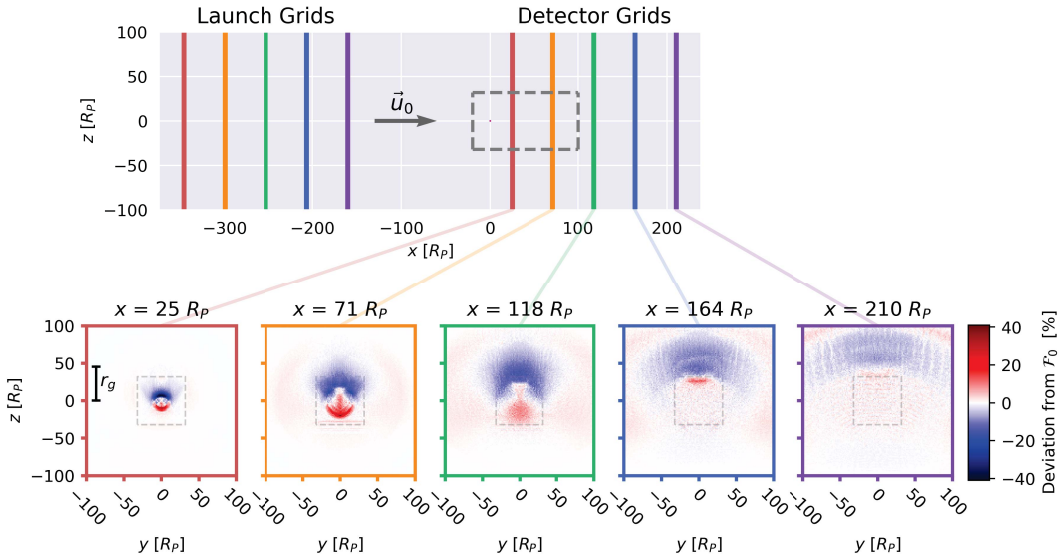

Figure 9. Dependence of the measured ion fluxes on the positions of the launch and detector grids. The figure depicts the locations of the grids (top) and the detector outputs (bottom) from five different runs of the energetic particle tracer (section 2.2) for He^+ ions at an initial energy of $E = 2$ keV. The ions are propagated through the draped fields from AIKEF. The diagram of the grid geometries includes Pluto at the origin (magenta), and the extent of the AIKEF cuboid in this plane is indicated by the dashed gray lines. The locations of the launch grid (left, vertical lines), detector grid (right, vertical lines), as well as the flux map (bottom) for each of the five runs are distinguished by color. In each run, the launch and detector grids are displaced by $d = u_0 P_0$; i.e., in the top panel, vertical lines of the same color are $u_0 P_0$ apart. Starting with a detector grid at $x = 25\ R_P$ (red, leftmost map), the two grids are incremented by a distance $u_0 P_0/8$ farther downstream (i.e., in the positive x direction) in each subsequent run. The maps show the percent change in flux from the value measured through the detector grid in uniform fields, $\mathcal{F}_0$. For $E = 2$ keV, this value reads $\mathcal{F}_0 = 2.32\ \mathrm{cm}^{-2}\ \mathrm{s}^{-1}\ \mathrm{keV}^{-1}\ \mathrm{sr}^{-1}$; this is the same for each of the five grid geometries since d does not change between the different setups. The projection of the AIKEF cuboid on each detector plane is outlined by the dashed gray lines; the AIKEF cuboid does *not* intersect the flux maps recorded for $x > 100\ R_P$. Red/blue regions indicate an increase/decrease in flux, respectively, compared to the (spatially constant) value that would be observed in uniform electromagnetic fields.

At $x = 118\ R_P$, the regions of perturbed flux continue to increase in area; this trend persists to the detector at $x = 210\ R_P$ where the region of decreased flux has be-

come an arc across the northern half-space. The cells on the detector grid with the greatest deviations in flux from $\mathcal{F}_0$ at $x = 210\ R_P$ see a maximum decrease by 9% and increase by 7%, having diminished from the respective extrema at $x = 25\ R_P$ of a 41% decrease and a 34% increase. Moving from left to right in Figure 9, we see an approximately exponential decay in the magnitude of the flux depletions (blue) with increasing distance to Pluto, such that the fluxes measured by the detector grids in these regions converge towards $\mathcal{F}_0$. Hence, just as observed by NH, our model results reveal a region of limited extension along the Sun-Pluto line where perturbations in energetic He^+ flux are observable. Analogous runs at initial energy $E = 10$ keV reveal the same "smearing out" of the features in the flux maps and a similar convergence towards $\mathcal{F}_0(E)$ with increasing distance to Pluto. Just as in Figure 6, the magnitude of the deviations in flux from $\mathcal{F}_0$ diminish with increasing initial energy E, regardless of the position of the detector grid.

Observations from PEPSSI suggest the depletion in energetic heliospheric He^+ flux to extend downstream to $x = 190\ R_P$; over this distance, the initial reduction seen close to Pluto experiences an exponential "refilling" back towards the nominal upstream value (Kollmann, Hill, Allen, et al., 2019). Our model reveals a similar behavior, with fluxes returning to their background values around $x \approx 210\ R_P$. In addition, our simulation captures both regions of depleted and enhanced energetic He^+ flux, suggesting that the observable perturbation pattern is strongly dependent on the spacecraft's trajectory downstream. NH approached Pluto from the Sun direction nearly within its orbital plane ($z \approx 0$), heading in the $(-y)$ direction and slightly northward (see Figure 1 of Bagenal et al. (2016)). Initially, PEPSSI measured an enhancement in He^+ differential intensity as it was at $x \approx 8\ R_P$ with a look direction nearly perpendicular to the upstream flow direction. Figure 3 of Kollmann, Hill, Allen, et al. (2019) illustrates that PEPSSI observed an order-of-magnitude decrease in the differential intensity of He^+ at all energies downstream of Pluto as it was between $x = 20\ R_P$ and $x = 80\ R_P$, which is much stronger than the greatest depletion in flux seen by our model (a decrease by 41% in the $E = 2$ keV plot of Figure 6). Along its trajectory, the points where NH would intersect the detector grids of Figure 9 do not solely exhibit depletions in flux within the same $x \in [20, 80]\ R_P$ interval: instead, the NH trajectory crosses the model detectors at $x = 25\ R_P$ and $x = 71\ R_P$ in regions of elevated He^+ flux. Nonetheless, this is qualitatively consistent with the initial enhancement in energetic He^+ flux observed by PEPSSI, prior

to the order-of-magnitude depletion, as it moved northward within the perturbed field region. However, the morphology of the perturbations in flux seen in Figures 6 and 9 is highly dependent on the strength and orientation of the IMF. If $\vec{B}_0$ were oriented oppositely (in the $+y$ direction) the features in our flux maps would be mirrored across the $z = 0$ plane; additionally, if the field magnitude differed from the value in our model ($|\vec{B}_0| = 0.24$ nT), the areas of perturbed flux would either grow or shrink with the ion gyroradii.

The energy-independence of the He^+ flux depletion observed by PEPSSI contrasts our model results, which reveal that deviations from the value in uniform fields, $\mathcal{F}_0$, diminish with increasing initial energy E (see Figure 6). This modeled behavior is plausible, since higher energy ions spend an increasingly smaller fraction of a gyration arc within the highly perturbed fields near Pluto. In other words, the "effective" size of the obstacle represented by the dwarf planet's induced magnetosphere decreases with increasing ion energy. In addition, the plots of the Lorentz force $\vec{F}_L$ in Figure 7 illustrate substantial deflection to occur only on length scales much smaller than the size of the induced magnetosphere. Hence, it becomes increasingly "difficult" for the field perturbations to deflect the higher energy ions from their nearly-ballistic trajectories (see Figure 8). This result is consistent with energetic ion behavior found at other small bodies: for instance, Liuzzo et al. (2019) traced Jovian magnetospheric protons with energies from 1 keV up to 5 MeV through the draped electromagnetic fields near Callisto (calculated using AIKEF). These authors demonstrated that the accessibility of Callisto's surface to such protons becomes increasingly uniform with greater energy, since the more energetic ions are only slightly deflected by the field perturbations. A similar behavior has been found for energetic ion motion through the draped electromagnetic fields near Europa (Addison et al., 2021; Nordheim et al., 2022; Haynes et al., 2023).

While this dependence of the magnitude of the flux perturbations on initial energy E seen in our model results is in agreement with energetic particle behavior near other small bodies, the PEPSSI instrument measured a *uniform* decrease in He^+ flux by a factor of ten across all energies from 2 keV to 100 keV (Kollmann, Hill, Allen, et al., 2019). Hence, our model results show that the interaction with a *steady-state* induced magnetosphere at Pluto cannot explain the magnitude of the decrease in He^+ flux recorded by NH, nor the energy-independence of the observed drop. A possible cause of this deviation are time-dependent processes (e.g., bi-ion waves; Delamere, 2009) within Pluto's

interaction region that cannot be emulated with our current model setup. As seen in the results of the test-particle model of Kollmann, Hill, Allen, et al. (2019), such waves can cause additional deflection of the energetic particles as they travel through Pluto's wake. However, accounting for energetic ion deflection by, e.g., bi-ion waves would entail outputting the three-dimensional electromagnetic field geometry from AIKEF at *multiple* points in time spanning the duration of the wave's travel through Pluto's wake region. The particle tracer would then need to sample consecutive field cubes at different times to emulate the wave's propagation through the perturbed fields. However, such an effort constitutes a separate, follow-up study. Quantitative discrepancies between our model output and observations may also stem from the fact that—due to computational constraints—we consider individual slices through the upstream ion population and do not sample it in its entirety (see section 2.3).

A direct comparison between our two-dimensional flux maps and PEPSSI observations is not feasible. Measurements of the energetic He^+ ions were obtained over dozens of R_P within the non-uniform fields downstream of Pluto, collected by an instrument field-of-view covering about 0.66 sr that was continuously rotating about the x-axis (Kollmann, Hill, Allen, et al., 2019). Since only a tiny fraction of the ions in our model domain would actually be captured by PEPSSI, attempting to reproduce its measurements would entail the use of a backtracing model. This approach would require launching energetic He^+ macroparticles from the momentary position of the instrument and accounting for the instantaneous orientation of its field-of-view at each point along the spacecraft's trajectory. The ions would be traced backward in time (i.e., with a negative timestep Δt) until they leave Pluto's interaction region or enter the dwarf planet's collisional lower atmosphere (see, e.g., Liuzzo, Poppe, et al., 2024; Liuzzo, Nénon, et al., 2024; Tippens et al., 2024). If an ion macroparticle reaches the uniform fields outside of Pluto's interaction region, its differential intensity can be sampled from the observed upstream distribution (Figure 3 of Kollmann, Hill, Allen, et al., 2019); the ion's contribution to flux at the location of the instrument can then be calculated via Liouville's theorem (equation (3)). Developing such a backtracing model will be the goal of our future work. Nevertheless, the two-dimensional model output of our current study provides important physical context for the interaction of energetic He^+ with Pluto's induced magnetosphere that could not be deduced from the observations along the New Horizons trajectory alone.

4 Summary and Concluding Remarks

In this study, we have investigated the effect of the draped electromagnetic fields in Pluto's induced magnetosphere on the distribution of energetic heliospheric He^+ ions. Our goal was to identify the physical mechanisms responsible for the depletion in He^+ flux observed downstream of Pluto by the PEPSSI instrument aboard NH (Bagenal et al., 2016; Kollmann, Hill, Allen, et al., 2019). To accomplish this, we employed the AIKEF hybrid model (Müller et al., 2011) for determining the three-dimensional structure of the draped electromagnetic fields near Pluto. The field output from AIKEF was then embedded in a newly developed particle tracing tool that propagates energetic He^+ ions through the dwarf planet's induced magnetosphere. Monoenergetic populations of such ions are initialized on a launch grid upstream of Pluto at various initial energies E (in the rest frame of the solar wind) within the range observed by PEPSSI. Their trajectories are traced through the perturbed fields near the dwarf planet using a combination of analytical and numerical methods, and their contributions to flux at the wake-side are recorded by a plane detector that is oriented perpendicular to the Sun-Pluto line. We have probed the three-dimensional structure of the patterns in He^+ flux by considering different distances between the detector grid and Pluto.

Ion gyroradii near Pluto are 1-3 orders of magnitude larger than the dwarf planet itself. Consequently, Pluto's induced magnetosphere is highly asymmetric in planes perpendicular to the IMF direction. Thus, Pluto presents a scenario in which the induced magnetosphere is shaped by large ion gyroradii, while observations suggest that it simultaneously has a drastic influence on the surrounding distribution of energetic heliospheric ions.

Our major results are as follows:

1. Pluto causes highly non-uniform perturbation patterns of the energetic He^+ flux in its wake. An IMF antiparallel to Pluto's orbital motion generates a downstream region of depleted flux through the detector grid in the northern half-space ($z > 0$), accompanied by a region of elevated flux to its south. This pattern persists across all initial He^+ energies from $E = 2$ keV to $E = 100$ keV. The maximum enhancement is about 41% above the unperturbed He^+ flux recorded by the detector grid in uniform fields, $\mathcal{F}_0$. The strongest depletion is a decrease by 34% of $\mathcal{F}_0$. With increasing distance between the detector and Pluto, these regions grow in

area while the perturbations weaken and the flux approaches $\mathcal{F}_0$. The modeled flux perturbations gradually disappear over a distance near 210 R_P downstream of Pluto, compared to the downstream extent of the energetic ion wake estimated from PEPSSI data of 190 R_P (Kollmann, Hill, Allen, et al., 2019).

2. The energetic He^+ trajectories are most significantly deflected in localized regions of the induced magnetosphere where the magnetic field magnitude shows the strongest enhancements above the background value. One of these regions is the magnetic pileup region that becomes stretched southward and downstream by the deflected solar wind. As an He^+ ion passes through this region, its gyroradius locally decreases, deflecting the ion away from the path it would have taken in uniform fields. Additionally, energetic He^+ trajectories experience strong perturbations when encountering regions of reduced electric field strength, such as within Pluto's heavy ion tail. The near-zero electric field deflects the ions by preventing them from being carried toward downstream by the $\vec{E} \times \vec{B}$ drift.
3. The modification of energetic He^+ flux through the detector grid depends on the ions' initial energy E in the rest frame of the solar wind. Specifically, the magnitude of the flux perturbations diminishes with increasing E. Because the energetic ion gyroradii exceed the size of Pluto by multiple orders of magnitude, the segment of an ion's trajectory within the perturbed fields becomes increasingly minuscule relative to the scale of their gyration with greater initial energy E. Thus, Pluto's induced magnetosphere becomes less "effective" in perturbing the trajectories of ions at higher energies. This behavior is consistent with expectations from models of energetic ion dynamics at other small bodies, e.g., Callisto and Europa (Liuzzo et al., 2019; Addison et al., 2021; Nordheim et al., 2022; Haynes et al., 2023).
4. Even at the lowest energy considered ($E = 2$ keV), the magnitude of the modeled drop in He^+ flux within Pluto's induced magnetosphere is more than a factor of five lower than observed by PEPSSI. Furthermore, this deviation grows with increasing ion energy: the perturbations to the modeled flux pattern gradually disappear as E grows. This quantitative discrepancy may partially stem from time-dependent processes that the steady-state field output from AIKEF does not capture, such as scattering of the energetic He^+ ions by plasma waves in Pluto's wake.

According to PEPSSI observations, Pluto's largest moon Charon seems to cause a localized perturbation in He^+ flux within the dwarf planet's wake (Bagenal et al., 2016).

Depending on its orbital phase with respect to Pluto, Charon may also have a discernible influence on the electromagnetic fields within the induced magnetosphere (Hale & Paty, 2017). The natural progression of this study will therefore also account for the presence of Charon when investigating the interaction of the Pluto system with energetic heliospheric ions.

Acknowledgements

The authors acknowledge financial support through NASA's *Solar System Workings Program* 2021, grant #80NSSC23K0352. This body of work was not written nor contributed to in any part by an artificial intelligence engine. The authors would like to thank both referees for careful inspection of the manuscript and for valuable comments.

Data Availability Statement

Data supporting the production and conclusions of this work can be obtained from Ruch et al. (2024).

References

Addison, P., Haynes, C. M., Stahl, A. M., Liuzzo, L., & Simon, S. (2024). Magnetic Signatures of the Interaction Between Europa and Jupiter's Magnetosphere During the Juno Flyby. *Geophysical Research Letters*, *51*(2), e2023GL106810. Retrieved from https://agupubs.onlinelibrary.wiley.com/doi/abs/10.1029/2023GL106810 (e2023GL106810 2023GL106810) doi: https://doi.org/10.1029/2023GL106810

Addison, P., Liuzzo, L., Arnold, H., & Simon, S. (2021). Influence of Europa's Time-Varying Electromagnetic Environment on Magnetospheric Ion Precipitation and Surface Weathering. *Journal of Geophysical Research: Space Physics*, *126*(5), e2020JA029087. Retrieved from https://agupubs.onlinelibrary.wiley.com/doi/abs/10.1029/2020JA029087 (e2020JA029087 2020JA029087) doi: https://doi.org/10.1029/2020JA029087

Addison, P., Liuzzo, L., & Simon, S. (2022). Effect of the Magnetospheric Plasma Interaction and Solar Illumination on Ion Sputtering of Europa's Surface Ice. *Journal of Geophysical Research: Space Physics*, *127*(2), e2021JA030136. Retrieved from https://agupubs.onlinelibrary.wiley.com/doi/abs/10.1029/2021JA030136 (e2021JA030136 2021JA030136) doi: https://doi.org/10.1029/2021JA030136

Addison, P., Liuzzo, L., & Simon, S. (2023). Surface-Plasma Interactions at Europa in Draped Magnetospheric Fields: The Contribution of Energetic Electrons to Energy Deposition and Sputtering. *Journal of Geophysical Research: Space Physics*, *128*(8), e2023JA031734. Retrieved from https://agupubs.onlinelibrary.wiley.com/doi/abs/10.1029/2023JA031734 (e2023JA031734 2023JA031734) doi: https://doi.org/10.1029/2023JA031734

Bagenal, F., Delamere, P. A., Elliott, H. A., Hill, M. E., Lisse, C. M., McComas, D. J., ... Strobel, D. F. (2015, September). Solar wind at 33 AU: Setting bounds on the Pluto interaction for New Horizons. *Journal of Geophysical Research (Planets)*, *120*, 1497–1511. doi: 10.1002/2015JE004880

Bagenal, F., Horányi, M., McComas, D. J., McNutt, R. L., Elliott, H. A., Hill, M. E., ... Zangari, A. M. (2016, March). Pluto' interaction with its space environment: Solar wind, energetic particles, and dust. *Science*, *351*, aad9045. doi: 10.1126/science.aad9045

Barnes, N. P., Delamere, P. A., Strobel, D. F., Bagenal, F., McComas, D. J., Elliott, H. A., ... Stern, S. A. (2019, March). Constraining the IMF at Pluto Using New Horizons SWAP Data and Hybrid Simulations. *Journal of Geophysical Research (Space Physics)*, *124*(3), 1568-1581. doi: 10.1029/2018JA026083

Coates, A., Rodgers, D., Johnstone, A., Smith, M., & Heath, J. (1988). Development of the first artificial comet: UKS ion measurements. *Advances in Space Research*, *8*(1), 15-21. Retrieved from `https://www.sciencedirect.com/science/article/pii/0273117788903377` doi: https://doi.org/10.1016/0273-1177(88)90337-7

Cravens, T., & Strobel, D. (2015). Pluto's solar wind interaction: Collisional effects. *Icarus*, *246*, 303 - 309. Retrieved from `http://www.sciencedirect.com/science/article/pii/S0019103514002036` (Special Issue: The Pluto System) doi: https://doi.org/10.1016/j.icarus.2014.04.011

Delamere, P. A. (2009, March). Hybrid code simulations of the solar wind interaction with Pluto. *Journal of Geophysical Research (Space Physics)*, *114*, A03220. doi: 10.1029/2008JA013756

Delamere, P. A., & Bagenal, F. (2004, February). Pluto's kinetic interaction with the solar wind. *Geophys. Res. Lett.*, *31*, L04807. doi: 10.1029/2003GL018122

Delamere, P. A., Swift, D. W., & Stenbaek-Nielsen, H. C. (1999). A three-dimensional hybrid code simulation of the December 1984 solar wind AMPTE release. *Geophysical Research Letters*, *26*(18), 2837-2840. Retrieved from `https://agupubs.onlinelibrary.wiley.com/doi/abs/10.1029/1999GL900602` doi: https://doi.org/10.1029/1999GL900602

Feyerabend, M., Liuzzo, L., Simon, S., & Motschmann, U. (2017). A Three-Dimensional Model of Pluto's Interaction With the Solar Wind During the New Horizons Encounter. *Journal of Geophysical Research: Space Physics*, *122*(10), 10,356-10,368. Retrieved from `https://agupubs.onlinelibrary.wiley.com/doi/abs/10.1002/2017JA024456` doi: 10.1002/2017JA024456

Fisk, L. A., & Gloeckler, G. (2012, November). Particle Acceleration in the Heliosphere: Implications for Astrophysics. *Space Sci. Rev.*, *173*, 433-458. doi: 10.1007/s11214-012-9899-8

Gladstone, G. R., Stern, S. A., Ennico, K., Olkin, C. B., Weaver, H. A., Young, L. A., ... Zirnstein, E. (2016, March). The atmosphere of Pluto as observed

by New Horizons. *Science*, *351*, aad8866. doi: 10.1126/science.aad8866

Hale, J. P. M., & Paty, C. S. (2017, May). Pluto-Charon solar wind interaction dynamics. *Icarus*, *287*, 131-139. doi: 10.1016/j.icarus.2016.11.036

Harnett, E. M., Winglee, R. M., & Delamere, P. A. (2005). Three-dimensional multi-fluid simulations of Pluto's magnetosphere: A comparison to 3D hybrid simulations. *Geophys. Res. Lett.*, *32*, L19104 (1–5), doi:10.1029/2005GL023178.

Haynes, C. M., Tippens, T., Addison, P., Liuzzo, L., Poppe, A. R., & Simon, S. (2023). Emission of Energetic Neutral Atoms from the Magnetosphere-Atmosphere Interactions at Callisto and Europa. *Journal of Geophysical Research: Space Physics*, *128*(10), e2023JA031931. doi: 10.1029/2023JA031931

Hubbard, W. B., Hunten, D. M., Dieters, S. W., Hill, K. M., & Watson, R. D. (1988, Dec). Occultation evidence for an atmosphere on Pluto. *Nature*, *336*, 452–454. doi: 10.1038/336452a0

Kollmann, P., Hill, M. E., Allen, R. C., McNutt Jr, R. L., Brown, L. E., Barnes, N. P., ... Stern, S. A. (2019). Pluto's Interaction With Energetic Heliospheric Ions. *Journal of Geophysical Research: Space Physics*, *124*(9), 7413-7424. Retrieved from `https://agupubs.onlinelibrary.wiley.com/doi/abs/10.1029/2019JA026830` doi: https://doi.org/10.1029/2019JA026830

Kollmann, P., Hill, M. E., McNutt, R. L., Brown, L. E., Allen, R. C., Clark, G., ... Szalay, J. R. (2019, may). Suprathermal Ions in the Outer Heliosphere. *The Astrophysical Journal*, *876*(1), 46. Retrieved from `https://dx.doi.org/10.3847/1538-4357/ab125f` doi: 10.3847/1538-4357/ab125f

Krasnopolsky, V. A. (1999, Mar). Hydrodynamic flow of N2 from Pluto. *Journal of Geophysical Research: Planets*, *104*(E3), 5955–5962. doi: 10.1029/1998je900052

Krasnopolsky, V. A., & Cruikshank, D. P. (1999, Sep). Photochemistry of Pluto's atmosphere and ionosphere near perihelion. *Journal of Geophysical Research: Planets*, *104*(E9), 21979–21996. doi: 10.1029/1999je001038

Liuzzo, L., Feyerabend, M., Simon, S., & Motschmann, U. (2015, November). The impact of Callisto's atmosphere on its plasma interaction with the Jovian magnetosphere. *Journal of Geophysical Research (Space Physics)*, *120*, 9401-9427. doi: 10.1002/2015JA021792

Liuzzo, L., Nénon, Q., Poppe, A. R., Stahl, A., Simon, S., & Fatemi, S. (2024). On the Formation of Trapped Electron Radiation Belts at Ganymede. *Geophysical Research Letters*, *51*(10), e2024GL109058. Retrieved from `https://agupubs.onlinelibrary.wiley.com/doi/abs/10.1029/2024GL109058` (e2024GL109058 2024GL109058) doi: https://doi.org/10.1029/2024GL109058

Liuzzo, L., Poppe, A. R., Nénon, Q., Simon, S., & Addison, P. (2024, Feb). Constraining the influence of Callisto's perturbed electromagnetic environment on energetic particle observations. *Journal of Geophysical Research: Space Physics*, *129*(2). doi: 10.1029/2023ja032189

Liuzzo, L., Simon, S., Feyerabend, M., & Motschmann, U. (2016). Disentangling plasma interaction and induction signatures at Callisto: The Galileo C10 flyby. *Journal of Geophysical Research: Space Physics*, *121*(9), 8677–8694. Retrieved from `http://dx.doi.org/10.1002/2016JA023236` doi: 10.1002/2016JA023236

Liuzzo, L., Simon, S., Feyerabend, M., & Motschmann, U. (2017). Magnetic signatures of plasma interaction and induction at Callisto: The Galileo C21, C22, C23, and C30 flybys. *Journal of Geophysical Research: Space Physics*, *122*(7), 7364–7386. doi: 10.1002/2017JA024303

Liuzzo, L., Simon, S., & Regoli, L. (2019). Energetic electron dynamics near Callisto. *Planetary and Space Science*, *179*, 104726. Retrieved from `http://www.sciencedirect.com/science/article/pii/S0032063319302430` doi: https://doi.org/10.1016/j.pss.2019.104726

McComas, D. J., Allegrini, F., Bagenal, F., Casey, P., Delamere, P., Demkee, D., ... et al. (2007, Aug). The Solar Wind Around Pluto (SWAP) Instrument Aboard New Horizons. *Space Science Reviews*, *140*(1–4). doi: 10.1007/s11214-007-9205-3

McComas, D. J., Elliott, H. A., Weidner, S., Valek, P., Zirnstein, E. J., Bagenal, F., ... Weaver, H. A. (2016). Pluto's interaction with the solar wind. *Journal of Geophysical Research (Space Physics)*, *121*(5), 4232–4246. (2016JA022599) doi: 10.1002/2016JA022599

McComas, D. J., Zirnstein, E. J., Bzowski, M., Elliott, H. A., Randol, B., Schwadron, N. A., ... et al. (2017, Nov). Interstellar Pickup Ion Observations to 38 AU. *The Astrophysical Journal Supplement Series*, *233*(1). doi:

10.3847/1538-4365/aa91d2

Müller, J., Simon, S., Motschmann, U., Glassmeier, K. H., Saur, J., Schuele, J., & Pringle, G. J. (2010). Magnetic field fossilization and tail reconfiguration in Titan's plasma environment during a magnetopause passage: 3D adaptive hybrid code simulations . *Planet. Space Sci.*, *58*(12), 1526–1546, doi: 10.1016/j.pss.2010.07.018.

Müller, J., Simon, S., Motschmann, U., Schüle, J., Glassmeier, K., & Pringle, G. J. (2011). A.I.K.E.F.: Adaptive hybrid model for space plasma simulations. *Computer Physics Communications*, *182*(4), 946–966, doi: 10.1016/j.cpc.2010.12.033.

Nilsson, H., Wieser, G. S., Behar, E., Gunell, H., Wieser, M., Galand, M., ... Vigren, E. (2017, 06). Evolution of the ion environment of comet 67P during the Rosetta mission as seen by RPC-ICA. *Monthly Notices of the Royal Astronomical Society*, *469*, S252-S261. Retrieved from `https://doi.org/10.1093/mnras/stx1491` doi: 10.1093/mnras/stx1491

Nordheim, T. A., Regoli, L. H., Harris, C. D. K., Paranicas, C., Hand, K. P., & Jia, X. (2022, January). Magnetospheric Ion Bombardment of Europa's Surface. *Planetary Science Journal*, *3*(1), 5. doi: 10.3847/PSJ/ac382a

Owen, T. C., Roush, T. L., Cruikshank, D. P., Elliot, J. L., Young, L. A., de Bergh, C., ... Bartholomew, M. J. (1993, Aug). Surface ices and the atmospheric composition of Pluto. *Science*, *261*(5122), 745–748. doi: 10.1126/science.261.5122.745

Parker, E. N. (1958, November). Dynamics of the Interplanetary Gas and Magnetic Fields. *The Astrophysical Journal*, *128*, 664. doi: 10.1086/146579

Randol, B. M., & Christian, E. R. (2014). Simulations of plasma obeying coulomb's law and the formation of suprathermal ion tails in the solar wind. *Journal of Geophysical Research: Space Physics*, *119*(9), 7025-7037. Retrieved from `https://agupubs.onlinelibrary.wiley.com/doi/abs/10.1002/2014JA020095` doi: https://doi.org/10.1002/2014JA020095

Regoli, L. H., Coates, A. J., Thomsen, M. F., Jones, G. H., Roussos, E., Waite, J. H., ... Cox, G. (2016). Survey of pickup ion signatures in the vicinity of Titan using CAPS/IMS. *Journal of Geophysical Research: Space Physics*, *121*(9), 8317-8328. Retrieved from `https://agupubs.onlinelibrary`

.wiley.com/doi/abs/10.1002/2016JA022617 doi: https://doi.org/10.1002/2016JA022617

Richards, P. G., Fennelly, J. A., & Torr, D. G. (1994). EUVAC: A solar EUV Flux Model for aeronomic calculations. *Journal of Geophysical Research: Space Physics*, *99*(A5), 8981-8992. Retrieved from https://agupubs.onlinelibrary.wiley.com/doi/abs/10.1029/94JA00518 doi: 10.1029/94JA00518

Ruch, R., Simon, S., & Haynes, C. M. (2024). Data for "Dynamics of Energetic Heliospheric Ions in Pluto's Induced Magnetosphere" by Ruch et al., 2024 [Data set]. *Zenodo*, https://doi.org/10.5281/zenodo.14052522. doi: 10.5281/zenodo.14052522

Schunk, R. W., & Nagy, A. F. (2009). *Ionospheres: Physics, plasma physics, and chemistry* (2nd ed.). Cambridge University Press.

Simon, S., Boesswetter, A., Bagdonat, T., Motschmann, U., & Glassmeier, K.-H. (2006). Plasma environment of Titan: a 3-d hybrid simulation study. *Ann. Geophys.*, *24*(3), 1113–1135.

Simon, S., Boesswetter, A., Bagdonat, T., Motschmann, U., & Schuele, J. (2007). Three-dimensional multispecies hybrid simulation of Titan's highly variable plasma environment. *Annales Geophysicae*, *25*(1), 117–144. Retrieved from https://angeo.copernicus.org/articles/25/117/2007/ doi: 10.5194/angeo-25-117-2007

Stahl, A., Addison, P., Simon, S., & Liuzzo, L. (2023, Dec). A model of Ganymede's magnetic and plasma environment during the Juno PJ34 flyby. *Journal of Geophysical Research: Space Physics*, *128*(12). doi: 10.1029/2023ja032113

Tippens, T., Liuzzo, L., & Simon, S. (2022, Oct). Influence of Titan's variable electromagnetic environment on the global distribution of energetic neutral atoms. *Journal of Geophysical Research: Space Physics*, *127*(10). doi: 10.1029/2022ja030722

Tippens, T., Roussos, E., Simon, S., & Liuzzo, L. (2024, Jan). A novel Backtracing model to study the emission of energetic neutral atoms at Titan. *Journal of Geophysical Research: Space Physics*, *129*(1). doi: 10.1029/2023ja032083

Valenzuela, A., Haerendel, G., Föppl, H., Melzner, F., Neuss, H., Rieger, E., ... Loidl, J. (1986). The AMPTE artificial comet experiments. *Nature*, *320*(6064), 700–703.

Young, L. A., Elliot, J. L., Tokunaga, A., de Bergh, C., & Owen, T. (1997, May). Detection of Gaseous Methane on Pluto. *Icarus*, *127*, 258-262. doi: 10.1006/icar.1997.5709

Young, L. A., Kammer, J. A., Steffl, A. J., Gladstone, G. R., Summers, M. E., Strobel, D. F., ... Versteeg, M. (2017). Structure and composition of Pluto's atmosphere from the New Horizons solar ultraviolet occultation. *Icarus*, *300*, 174 - 199. Retrieved from `http://www.sciencedirect.com/science/article/pii/S0019103517302609` doi: https://doi.org/10.1016/j.icarus.2017.09.006

Zirnstein, E. J., McComas, D. J., Elliott, H. A., Weidner, S., Valek, P. W., Bagenal, F., ... Young, L. A. (2016, June). Interplanetary Magnetic Field Sector from Solar Wind around Pluto (SWAP) Measurements of Heavy Ion Pickup near Pluto. *The Astrophysical Journal*, *823*, L30. doi: 10.3847/2041-8205/823/2/L30